Article

DcAFF (Discontinuous Aligned Fibre Filament) – Investigation of Mechanical Properties of Multilayer Composites from 3D Printing

Narongkorn Krajangsawasdi [1,*], Fernando Alvarez-Borges [2], Keiran M. Ball [2], Mark N. Mavrogordato [2], Ian Hamerton [1], Benjamin K.S. Woods [1], Marco L. Longana [1,#] , and Dmitry S. Ivanov[1]

[1] Bristol Composites Institute, Department of Aerospace Engineering, University of Bristol, Queen's Building, University Walk, Bristol BS8 1TR, UK; ian.hamerton@bristol.ac.uk (I.H.), ben.k.s.woods@bristol.ac.uk (B.W.), dmitry.ivanov@bristol.ac.uk (D.M.).

[2] µ-VIS X-ray Imaging Centre, Faculty of Engineering and Physical Sciences, University of Southampton, University Road, Southampton SO17 1BJ; f.j.alvarez-borges@soton.ac.uk (F.A.), mnm100@soton.ac.uk (M.M), k.ball@solton.ac,uk (K.B)

[#] Current affiliation: Department of Chemistry, Materials and Chemical Engineering "Giulio Natta", Poli-tecnico di Milano, Piazza Leonardo da Vinci 32, 20133 Milan, Italy; marcoluigi.longana@polimi.it (M.L.L.)

* Correspondence: ih18506@bristol.ac.uk

Abstract: DcAFF (Discontinuous Aligned Fibre Filament) is a novel thermoplastic filament developed for fused filament fabrication (FFF)/ 3D printing. This filament is reinforced with highly aligned discontinuous fibres and is based on the High Performance Discontinuous Fibre (HiPerDiF) method which produces thin flat tapes suitable for a range of different composite manufacturing processes. The HiPerDiF, using fibres longer than the critical length, provides mechanical performance comparable to continuous fibre composites with the high formability typical of short fibre composites. Thanks to the development of the third-generation HiPerDiF machine and the DcAFF filament forming method, circular DcAFF filaments can be produced consistently and at high rates. In this paper, both the physical properties and the internal architecture of the produced filament were investigated. In particular µCT scanning and image post-processing were used to quantify fibre alignment. The designed filament-forming process ensures that the large fraction of the fibres in the final product are well aligned with the longitudinal axis of the filament. The mechanical properties of the multilayer DcAFF 3D printing part are presented for the first time in this paper with tensile, short beam shear (SBS), and open-hole tensile testing. The comparison with the previous studies and data in the literature shows comparable or indeed superior performance of DcAFF over existing methods for 3D printing composite parts, paving the way for this material as a candidate for high-performance 3D printing.

Keywords: Additive layer manufacturing, Multilayer 3D printing, Fused Filament Fabrication, Aligned Discontinuous Fibre, Thermoplastic, Tensile testing, Short beam shear testing, Open hole tensile testing

1. Introduction

Additive layer manufacturing (ALM), a layer-by-layer building technique, is a new generation of manufacturing approaches that allows to automate currently labour-intensive operations [1-3]. 3D printing, or Fused Filament Fabrication (FFF), is a type of ALM that fuses a solid polymer filament in a heated nozzle before depositing the molten polymer through a fine-diameter nozzle onto a bed, or the previously deposited layer, following a defined path [4-6]. With this automated layer-by-layer building procedure, complex geometries can be built at a lower cost, waste, labour, and time compared to conventional material removal processes [3,6,7]. Typically the polymers used for FFF are thermoplastics, *e.g.* poly(acrylonitrile-butadiene-styrene) (ABS), poly(L-lactic acid) (PLA), or polyamides (nylon, PA), because of the ease of reshaping them at low temperatures [8-10]. Nevertheless, the commonly used FFF thermoplastics have relatively low mechanical properties, so they need reinforcement to reach the performance requirement of primary structures [6,10-12]. A novel fibre architecture named Aligned Discontinuous Fibre Composites (ADFRCs), obtained with the High Performance Discontinuous Fibre (HiPerDiF) method was adapted to FFF by preparing new material forms [13-15]. ADFRCs produced with HiPerDiF allow to achieve mechanical performances comparable to continuous fibre composites [16] since the fibres are highly aligned and longer than the critical length (between 3 and 12 mm) while retaining the high processability/formability typical of short fibre composites [17].

Previously it was demonstrated in [16] that the HiPerDiF fibre preform can be deployed in 3D printing. The discontinuous fibre preform was impregnated with PLA in the form of a wide and thin film with a cross-section of 5 mm x 0.2 mm and then reshaped to a circular cross-section (1 mm diameter) using a specially designed bulking machine followed by a pultrusion process [16]. In the first series of manufacturing trials, the HiPerDiF-PLA tapes were produced using the second-generation lab-scale HiPerDiF machine. 3D printing filament, known as DcAFF (Discontinuous Aligned Fibre Filament), was printed in a single layer to assess the basic mechanical properties of the produced material. This study aims at extending the assessment by bringing together the improved HiPerDiF material forms and examining the properties of more representative multilayer configurations.

Currently, the third generation machine (HiPerDiF 3G) housed at the National Composites Centre, UK, can produce a higher throughput of HiPerDiF preform (metres per minute). More complex geometries and multilayer specimens can be printed to study various aspects of the DcAFF material performance. Figure 1 shows the schematic of the current HiPerDiF machine including the three modules: (i) the fibre-water mixing where the fibres are suspended in water with a defined concentration; (ii) the alignment where the fibres are sprayed to the alignment head; and (iii) the impregnation where the dry preform is coupled with the selected matrix.

This paper will initially focus on the DcAFF filament properties: fibre content and alignment calculated throughout the filament production process. Then, the mechanical performance of multilayer parts 3D printed with DcAFF material will be investigated. The mechanical testing of the DcAFF multilayer printed material includes (i) tensile testing, (ii) short beam shear testing (SBS) and (iii) open-hole tensile testing. Although there are some tests on the tensile and open-hole samples of DcAFF 3D printed material in the previous publications [16], they were focused only on the single-layer part which cannot fully represent the actual behaviour of the 3D printed part that may show some interaction between layers. This paper is the first time those properties and behaviour were studied with the full actual structure as multi-layer and compared with the DcAFF single-layer part or other composite 3D printing.

Figure 1 Schematic of the third generation HiPerDiF machine developed by the University of Bristol and located at the National Composites Centre, UK.

2. DcAFF filament quality

2.1. DcAFF filament production

In this study, the DcAFF material was composed of the combination of the Toho Tenax 3-mm chopped carbon fibre, 7 µm diameter and coated with water-soluble sizing and poly(L-lactic acid) – biopolymer (PLA) matrix, supplied as a roll of 0.05 mm thick film by Goodfellow Cambridge Ltd. After the HiPerDiF alignment process, the dry preform was merged with the PLA film with pressure around 1 bar at 200°C to ensure the fibres are well-impregnated with the matrix. The 32 mm wide composite tape was slit into 6-7 mm wide tapes. Then, the slit tape was reshaped into a 3D printing filament with the purposely built machine described in [16]. The tape was firstly compressed into a square-like cross-section (Figure 2(a)) in the small gap between two counterrotating and interlocking aluminium rollers. Then, the square filament was pultruded through a series of brass nozzles and finally a PTFE one to produce a circular filament with a diameter of 0.8 mm (Figure 2(b)) that is ready to be used with a standard 3D printer.

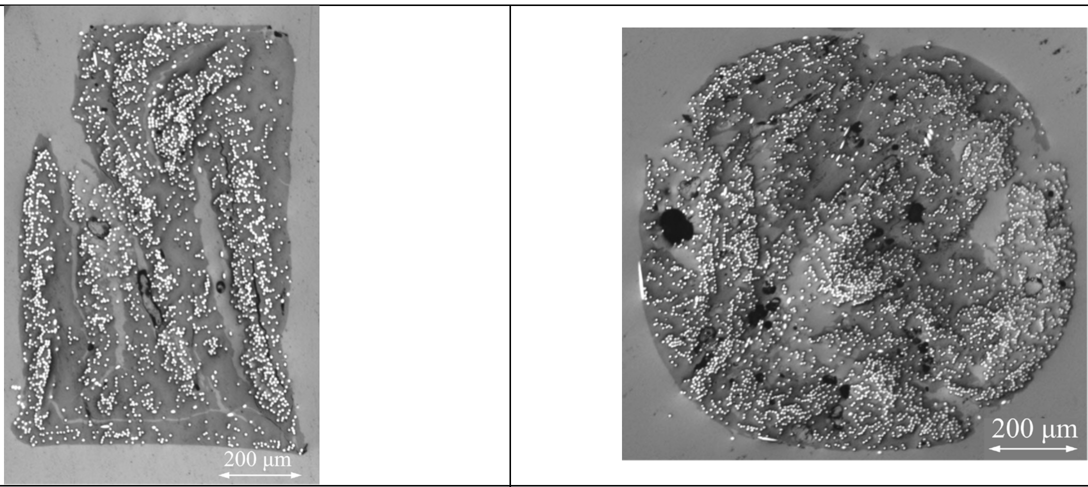

(a) (b)

Figure 2 Cross-section microscopy of (a) square-like filament after the compression process in a designed bulking machine; (b) final circular filament ready to use in a 3D printer.

2.2. *DcAFF filament fibre content measurement*

Fibre content was measured with the matrix burn-off procedure following the specific procedure for composite materials [18]. The sample was heated rapidly to 250°C with a 20°C/min ramp followed by a 10°C/min heating rate to 600°C and then held isothermally for 40 minutes. Besides the produced HiPerDiF-PLA composite filament and samples from printed parts, the raw materials (*i.e.* dry fibre and PLA) were also tested using the same programme to verify their residual mass after the dwelling stage. Figure 3 shows the result of the TGA programme, from which can be inferred that there is no significant amount of fibre burn-off and a very small amount of residual pure PLA after the process, so the residual of the fibre and PLA can be ignored from the fibre content calculation. In this current filament batch, the fibre weight content ranges between 21-30% in different sections of the filament and the printed part. The fibre content depends on the quality of the alignment process that feeds the fibre to the alignment head and conveyer belt. The fibre content of the material produced with the HiPerDiF 3G was intentionally kept slightly lower than the one produced with the second-generation lab-scale machine (approximately 28-32 % by weight) [15] with the intention to increase the amount of matrix in the composite to improve the adhesion of the filament to the printing bed and adjacent rasters. This fibre content calculation is purely based on the fibre weight, so there is no clear calculation on the micro-void fraction presented in the filament as seen in Figure 2, but the void (dark spots) on the cross section can be estimated with the nominal diameter of filament using the image-processing method presented in [14] accounting for less than 5% void in the cross-section volume.

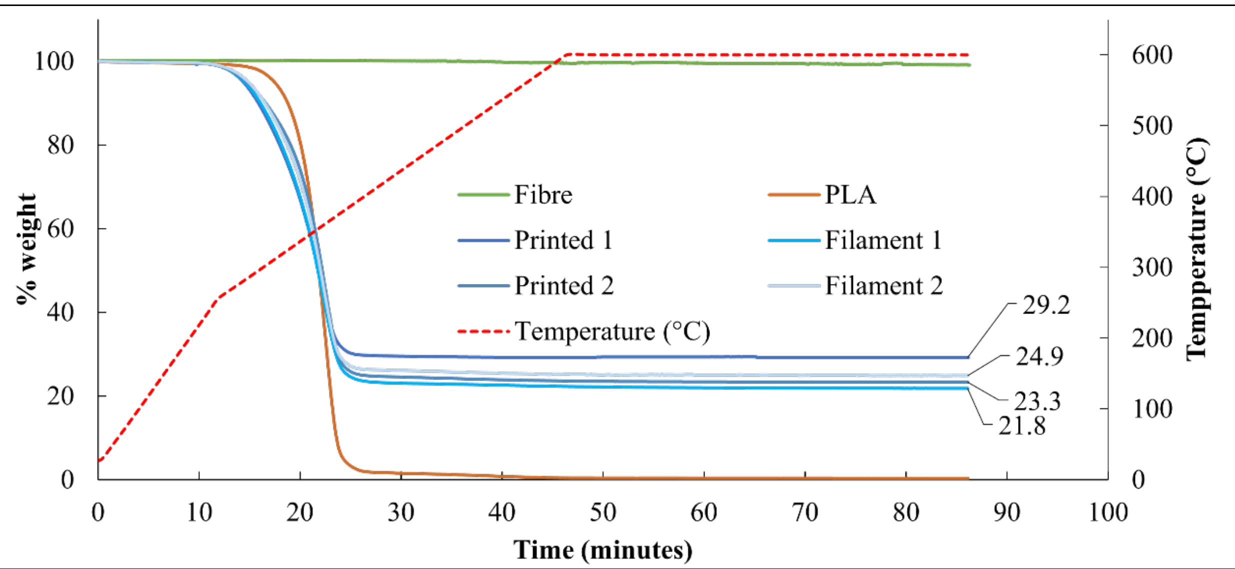

Figure 3 TGA result with matrix burn-off procedure of DcAFF filament showing with raw material, fibre, and PLA

2.3. *DcAFF filament fibre alignment angle measurement*

To understand the performance of DcAFF material, the alignment of the discontinuous fibre needs to be verified. In the first study of the HiPerDiF 3D printing filament forming [14], the alignment was measured from a single microscopic image of the specimen cross-section. Assuming that the cross-section is perfectly perpendicular to the 0° direction, the perfectly aligned fibres will appear as perfectly circular, but the misaligned ones will present an elliptical cross-section. The size of the elliptical shape, major and minor axes, were calculated and converted into the misalignment angle from the longitudinal axis *via* a trigonometric method. This method is cumbersome and time-consuming and allows the researcher to measure only a few cross-sections along the whole filament length, making it relatively unrepresentative and inaccurate. The second alignment measurement technique was based on the image analysis of a polished in-plane surface of the HiPerDiF tape. The method can evaluate only the in-plane fibre orientation of the through-thickness polished surface [19]. This is not suitable for the three-dimensional shape of the filament produced in this work. To measure the fibre alignment throughout the whole filament length, a higher-fidelity method is required. Microfocus X-ray computed tomography (μCT) is a suitable tool to analyse the whole structure of the material. It can separate the different materials (different densities), in this case, fibre, matrix and voids, to different greyscale and reconstruct a 3D image of the whole specimen. In a previous study [20], HiPerDiF tape fibre orientation was analysed with μCT scanning and the scanned images were processed using VoxTex software [21] developed at KU Leuven originally designed for the analysis of textile architectures. In this study, the orientation was analysed with commercial software, AVIZO with its extension X-Fibre, which can detect fibre or tube-like structures and calculate the orientation of each tube with respect to a defined set of coordinates [22].

The DcAFF material was scanned using a Zeiss 160 kVp Versa 510 μCT scanner. The source voltage was set at 80 kVp and 7 W power. 2401 projections with a 3-second exposure time per projection were acquired over a 360° rotation of the tomography stage, using a 4× magnification optics module. The source-to-object and object-to-detector distances were 24 mm and 16.4 mm, respectively, resulting in a 2 μm reconstructed voxel size. This resolution permitted resolving individual fibres, 7 μm in diameter. Each μCT acquisition consisted of four vertically overlapping scans to obtain a 3×3×12 mm^3 field of view that could cover more than a whole fibre length (3 mm). The same length of sample has been analysed through the three stages of the filament-forming process: tape, square-like filament, and circular filament to show the development of the fibre orientation during the filament-forming process. The tape was fitted in a clear tube which was then attached to the tomography stage. After scanning, the 3D images were analysed in AVIZO using the X-Fibre extension. First, the composite material was segmented to separate fibre and matrix depending on the grey scale of the scanned images, then a cylinder correlation module was applied to the stacked image to find the cylindrical volumes, supposed to be fibres. After that, the fibre tracing was applied to the cylinder correlation data to convert the traced cylinder into position and orientation data of each fibre by tracing the centre line of the cylinder. The orientation was calculated in reference to the axis shown in Figure 4(a). In this analysis, the interesting value is the fibre orientation angle θ which is the deviation angle from the longitudinal axis. However, two cylindric-shaped volumes of similar grey scale can be present in the scanned volume: real fibres, and, especially on the edge of the specimen, long cylindrical "channels" of matrix, denoted here as "fibre-like matrix artefacts". To avoid misinterpretation, the "fibre-like matrix artefacts" had to be filtered out from the tracing data accordingly to the following assumptions:

- Short fibres are rigid, no fibres with pronounced curvature can be presented in the scanned material;
- For the cylindrical shape filament (square or circular), there is a limit of fibre misalignment dictated by the size of the filament: in this case, the 1-mm filament diameter can provide room for 3-mm long fibre to deviate from the longitudinal axis no more than 28°;
- Fibre length limitation from the 3-mm input fibre:
    - The fibre cannot be extended: the maximum admissible fibre length is 3.5 mm;
    - The fibres are not broken during the process: the minimum admissible fibre length is 2.5 mm.

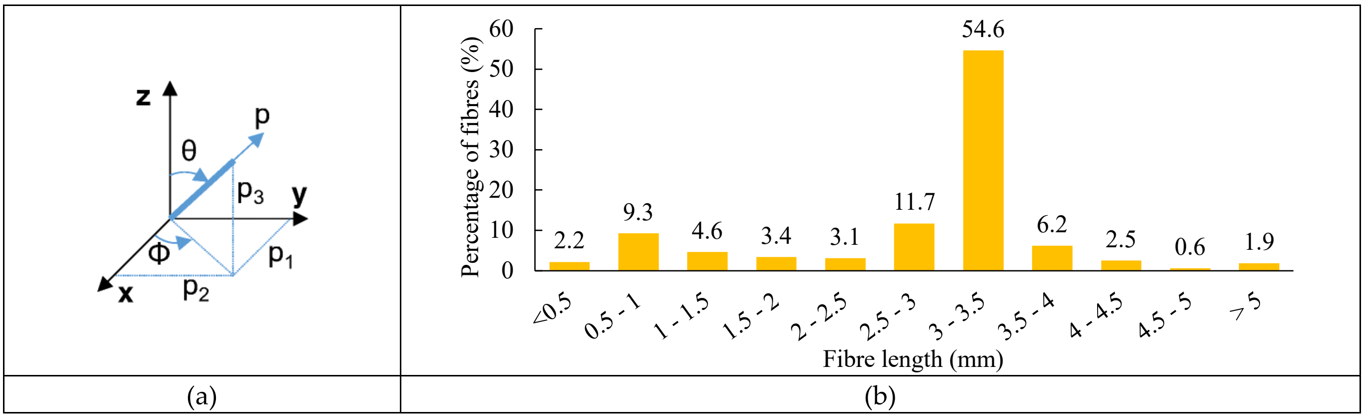

Figure 4 (a) Reference axis to calculate the fibre orientation; (b) FASEP fibre length measurement distribution of fibres processed from the HiPerDiF 3G machine.

The traced cylindrical volumes were filtered retaining those with a length between 2.5-3.5 mm which is the fibre following the given assumptions. The fibre length range assumptions were confirmed with FASEP system (IDM Systems, Darmstadt, Germany) [23], an image-processing fibre length measurement. Fibres extracted from a dry preform created with the HiPerDiF process were dispersed in water to be photographed through a flatbed scanner on the FASEP machine. The image was analysed by separating the single fibre from clusters and their length was automatically measured using a straight-fibre algorithm by FASEP software. The fibre length distribution after the HiPerDiF process, in Figure 4(b), confirms the assumption of fibre length distribution between 2.5-3.5 mm by showing the majority of the fibres are around 3 mm with an insignificant number of fibres in the other fibre length range. Due to the image processing method, the very low and high fibre length could be the noise (non-fibre voxels of similar grey-scale) from the measurement system.

The percentage of the number of fibres that deviated from the longitudinal axis was plotted in three histograms as a function of θ, for the different filament formats: tape, square, and circular in Figure 5(b), (d), and (f), respectively. According to those three histograms, most of the fibres are aligned within the range of 0-15°. Overall, the amount of perfectly aligned fibres (0° -1°) is lower than that of slightly misaligned ones (2-5°). The tape format may have a slightly higher misalignment because of the lesser geometrical constraint of the thin and wide tape, 32 mm in width, so the aligned 3-mm fibres on the tape surface can be easily deviated by the impregnation and forming process. This is shown by the misaligned fibre on the tape surface in Figure 5(a). However, the misalignment is significantly reduced due to the filament-forming process that forces all the fibre to align in one direction by compressing the tape to a constrained cross section, 1 mm x 1 mm, so the 3-mm-long fibre cannot deviate out of this boundary. In the square-like filament, the majority of fibres are well-aligned and the amount of fibres aligned over 15° is just 2%. The higher amount of aligned fibre can be seen in the 3D rendered image of the square filament, Figure 5(c). After the final pultrusion, the fibre orientation shows insignificant changes from the previous stage. The cross-section transformation after pultrusion into the circular filament is more uniform in shape compared to the square filament. The alignment level of each stage of the filament-forming calculated by the amount of the fibre aligned within 10° is presented in Table 1. The HiPerDiF tape produced by the HiPerDiF 3G machine shows a fibre alignment similar to that of the second-generation lab-scale machine (HiPerDiF 2G) measured in [20], *i.e.* 67% of fibre aligned within 10°. The filament-forming process provides a significant alignment improvement with about 90% of the fibre within 10°.

Table 1 Fibre alignment comparison over the development of DcAFF form tape to circular filament

Format	**Alignment (within 10°)**
Tape	63.7%
Square-like filament	89.0%
Circular filament	87.7%

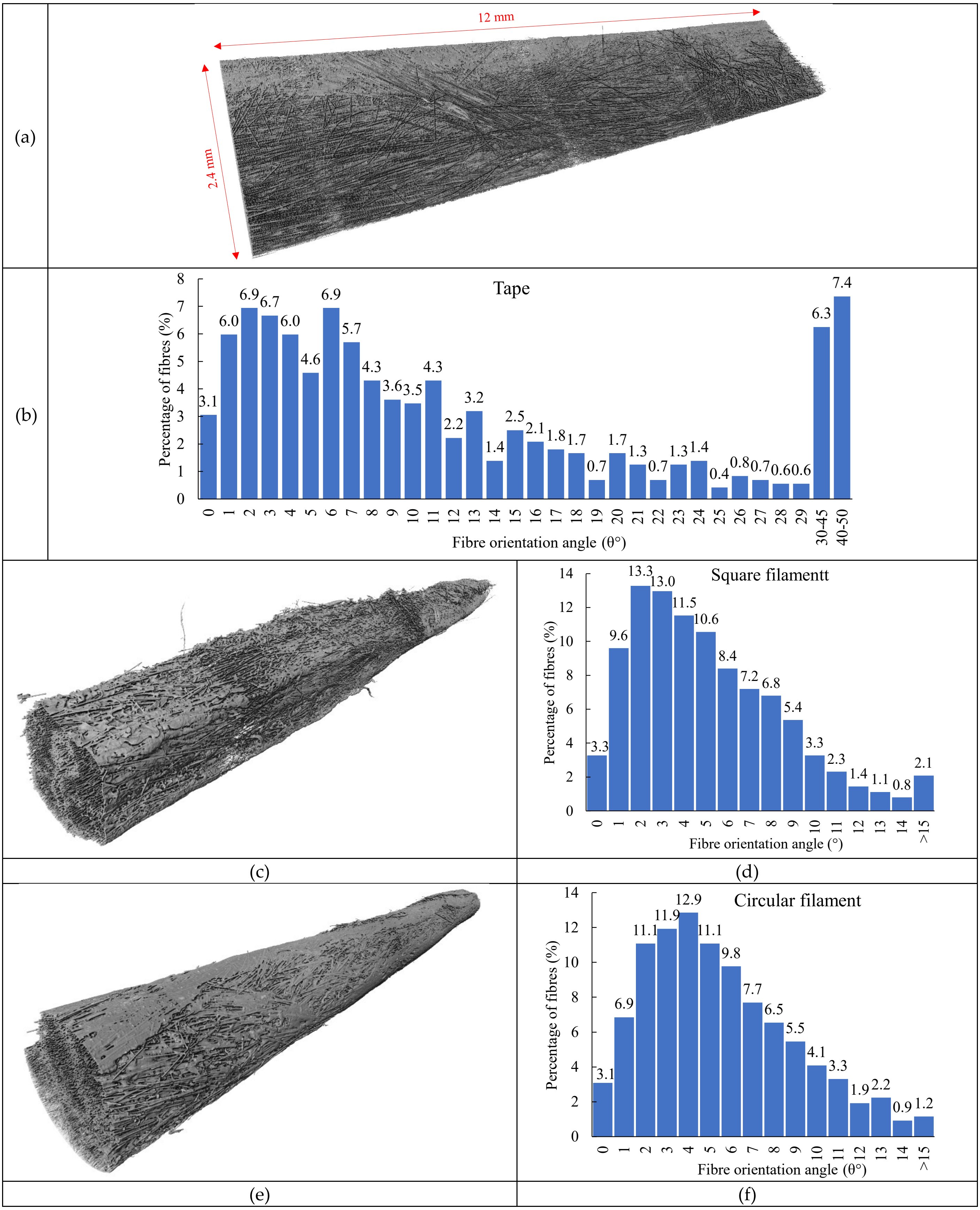

Figure 5 (a), (c), (e) 3D modelling of the µCT scanned image for cropped tape (2.4 mm wide), square-like filament and circular filament; (b), (d), (f) fibre orientation angle distribution deviation from the longitudinal axis.

3. Mechanical properties test

After the DcAFF material is formed into a circular cross-section and wound into a filament, it is ready to be printed into a defined shape. In the following tests, the samples were fabricated with a commercial Ender3 3D printer. The standard printer nozzle was substituted with one specifically designed for the discontinuous fibre composite filament, as detailed in [14]. The nozzle is machined from a hexagonal brass tube to a 1.4 mm diameter bore with a 1.25-mm-radius fillet edge around the nozzle outlet that allows the fibre to gently rotate from the vertical feeding direction to the horizontal printing bed. The printer was set up to the following parameters obtained from a previous study [14]: nozzle temperature 210°C, bed temperature 80°C, speed and feed rate 300 mm/min, and set nozzle height 0.3 mm. The raster gap was calculated based on the expected compacted area of the 0.8 mm diameter filament with 0.3 mm nozzle height based on the rectangular shape presenting about 1.6 mm raster width which can refer to the distance between the centre of the adjacent rasters.

3.1. Multi-layer Tensile testing

3.1.1. Tensile specimen preparation and testing procedure

The 3D printing path for tensile specimens was designed to be a 100-mm long concentric path, with four spiralling rasters for each layer, and built up to four layers. This is done *via* continuous printing by moving the nozzle 0.3 mm upwards at the end of each layer. The printing of the following layer started immediately after, and the raster was placed on top of the previous layer. The printing path of the four layers is shown in Figure 6(a). The top and bottom surfaces of the tensile specimen printed following the defined path are shown in Figure 6(b). When investigating the cross-section of the specimen (Figure 6(c)), the imperfect bonding between the adjacent rasters can be seen, especially the top surface that has only one round of nozzle compaction. While better inter-raster bonding was observed on the bottom layer thanks to the four cycles of compaction by the nozzle. Although the nozzle is able to provide a certain degree of compaction, the bonding between layers is still imperfect, as shown by the presence of some interlayer voids – Figure 6(c).

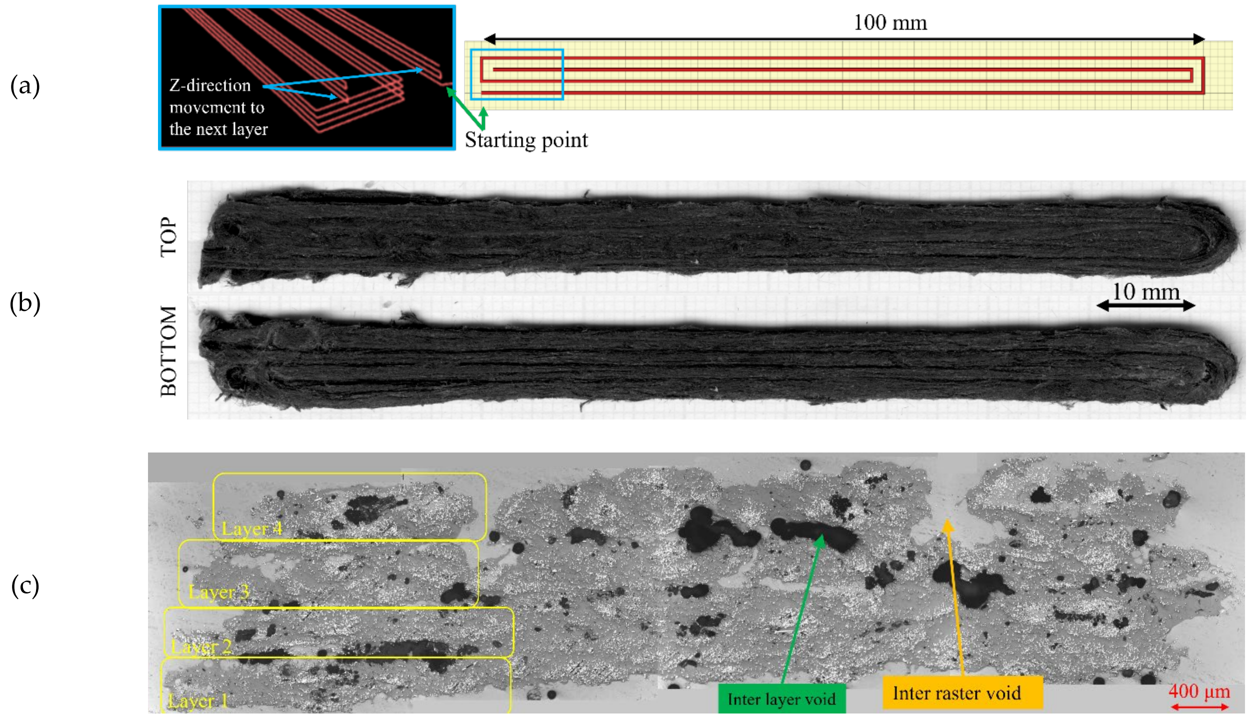

Figure 6 (a) Printing path for 4-layer stacking tensile specimen; (b) top and bottom surface of an actual 100-mm-long tensile specimen, (c) cross-section of the printed part showing four layers with four adjacent rasters on each layer.

To investigate the possibility of improving the mechanical properties through post-printing compaction, as done by some commercial solutions [24], a group of 3D printed samples was vacuum-bagged and heated to 200°C for 1 hour. This changes the sample morphology, improving the contact between adjacent rasters and surface finishing, as shown by the comparison in Figure 7(a). Moreover, the cross-section of the consolidated specimens is more uniform with fewer inter-raster voids than the as-printed part, as seen in the consolidated cross-section of Figure 7(b). To prevent material flow during the compaction, the specimens are placed in an open mould with a dam on the edges, this causes a slightly uneven cross-section with a higher thickness on the outer edges compared to the middle of the specimen.

The width and thickness of the specimen were measured at five positions across the length with a calliper and a micrometre, respectively. The average width and thickness of the as-printed are 6.94± 0.074 and 1.48±0.065 mm, respectively. The dimension change due to the consolidation was recorded as 7.02±0.23 mm in width and 1.45±0.12 mm in thickness from the part before the consolidation to 7.53±0.15 mm in width and 0.99±0.21 mm in thickness after the consolidation. The consolidation reduces the thickness, but increases the width of the specimen, so the average volume reduction is about 26% from the part before the consolidation, this could be attributed to voids removal.

The tensile samples were provided with 20-mm-long end-tabs at both ends leaving a 60-mm gauge length. There were five samples per test. The tensile testing was performed by a servo-electric tensile testing machine (Shimadzu, Japan) with a 1 kN load cell operated at a cross-head displacement speed of 1 mm/min and the strain was measured using a video extensometer (Imetrum, UK). The load, displacement, strain, and failure of the sample were recorded.

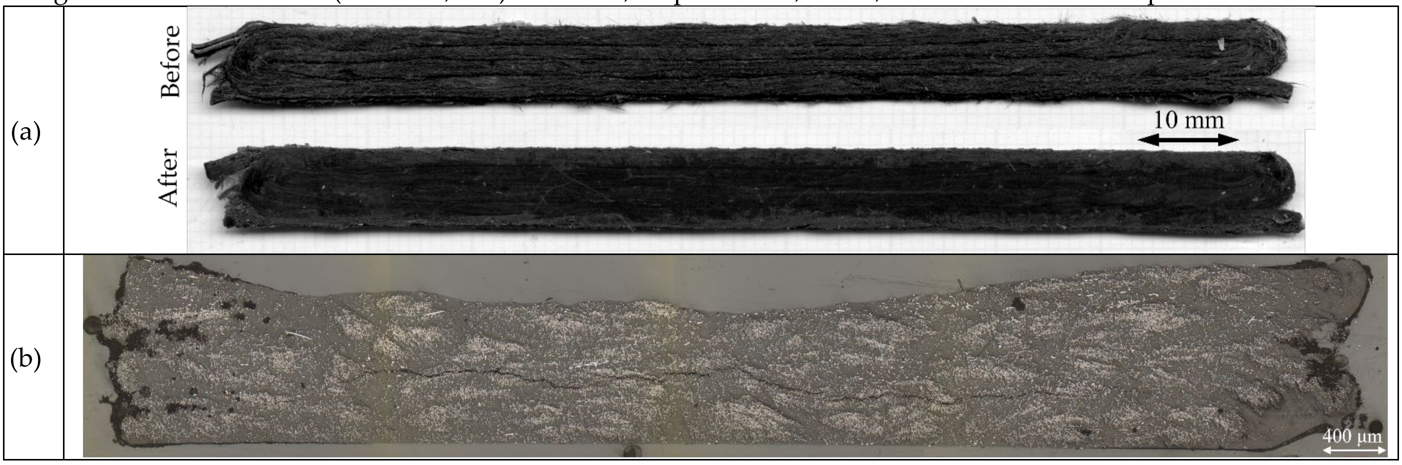

Figure 7 (a) comparison of the tensile specimen before and after post-printing consolidation; (b) cross-section of the tensile specimen after post-printing consolidation (the cross section microscopic image was taken after the tensile testing).

3.1.2. Tensile testing result

The tensile testing result is presented as a stress-strain curve in Figure 8(a). The DcAFF shows a brittle behaviour under tensile load, as seen in the linear curve until the breakage. The post-printing consolidation increases the tensile properties of the 3D printed sample, *i.e.* stiffness from 27.2 GPa to 43.6 GPa (about 60%) and strength from 184.0 MPa (~1895 N failure load) to 267.8 MPa (~2000 N failure load), accounting for about 45% increase, as seen in Figure 8(b) and (c). According to the low increase in the failure load of the compacted sample (only 5% from the as-printed), the property improvement is mainly the result of the cross-section area reduction from the elimination of the voids or other defects that improves the bonding between the raster/layer. SEM images in Figure 9 show the fracture surface of the tensile specimen with and without consolidation. In Figure 9(a), the as-printed specimen fracture surface presents a layer separation due to the poor bonding between layers; by contrast, the consolidated part shows a united structure. In both samples, there is no clear evidence of fibre breakage. The presence of "clean" fibres with no traces of resin on the fracture surface suggests that the major failure mechanism is fibre pull-out.

In Figure 10, the DcAFF as-printed part was compared to other 3D-printed tensile specimens from the literature, the collection of data, including the material used, fibre content, tensile stiffness and strength, can be seen in Appendix A. The DcAFF has significantly better mechanical properties than the neat PLA. In the reference studies reporting the results for reinforced filaments, the fibre content varied due to different manufacturing techniques. Short fibre composites showed consistently lower fibre volume fraction than DcAFF (5-20%), and composites with continuous fibres achieved higher volume fraction (up to 40-50%) - Table A3. Owing to the difference in the fibre content in each study, the literature data were normalised with the average fibre weight content of the current DcAFF at 25%.

When normalising the data, the strength of the short fibre composite increases up to the level of the DcAFF, this is because of the low fibre content in the short fibre-filled composite, *i.e.* 5-20%. However, on a practical level, it would be extremely difficult, if not impossible, to increase the short fibre content to 25% since the randomly aligned short fibres will cause nozzle clogging during printing. The stiffness of DcAFF material is significantly higher than the short fibre because of the alignment and the 3-mm long longer fibre which can carry and transfer the load better than fibres with length below 1 mm. When comparing the multilayer DcAFF to the single-layer 3D printed part of previous work [16], the multilayer printed material has higher stiffness and strength: this is the result of a better load-bearing capability given by more integrated rasters.

Comparing the multilayer DcAFF printed part to continuous fibre PLA composite which, on the contrary, has been scaled down, reveals that the DcAFF material has higher stiffness after normalisation, whereas the strength is lower. It can be inferred that the fibres used in the HiPerDiF process, which are close to the critical fibre length, plus the high alignment, are sufficient to provide mechanical properties comparable to a continuous fibre composite. Furthermore, it is likely that the performance of the DcAFF filament can be improved further if the fibre content increases. Unlike the case of randomly aligned fibres, the fibre volume fraction of the aligned fibre in the DcAFF can be boosted further towards the limit of the packing efficiency. This, in turn, offers a lower possibility for nozzle clogging, although this still requires some issues with the porosity of the filaments. Comparison of strengths is less straightforward as the performance of the matrix and fibre-matrix interface plays a more substantial role. The published results show the performance of the material with nylon matrix, whereas the current study operates with PLA. The high degree of hydrogen bonding present in nylon generally makes its performance superior.

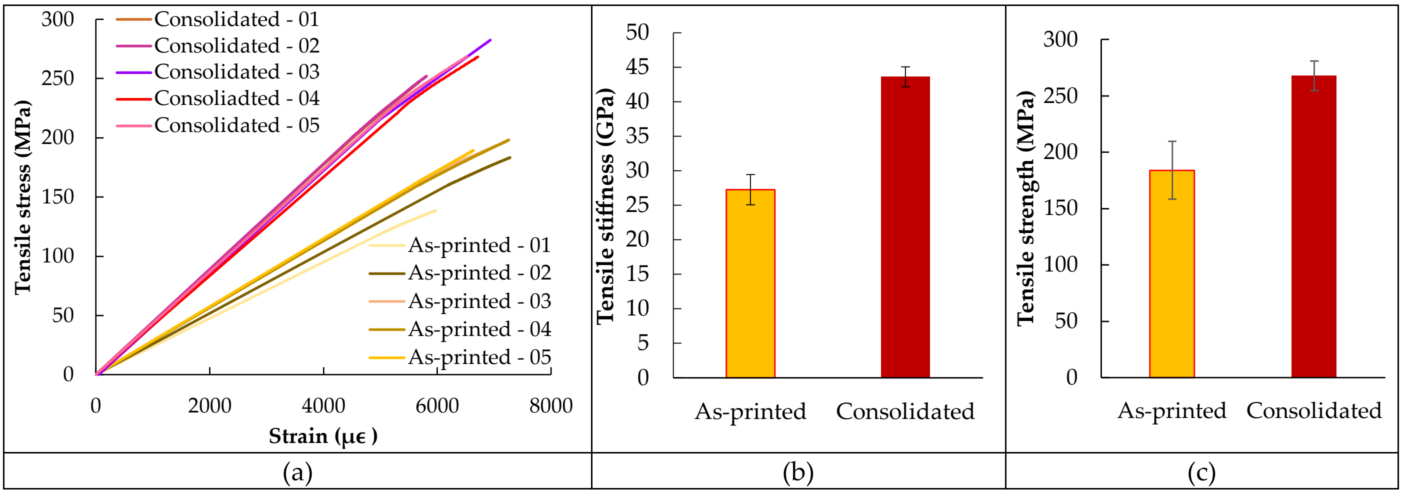

Figure 8 (a) Tensile stress-strain curve of the as-printed and consolidated specimens; comparison of as-printed and consolidated (under heat and pressure) tensile testing mechanical properties: (b) tensile stiffness; (c) tensile strength.

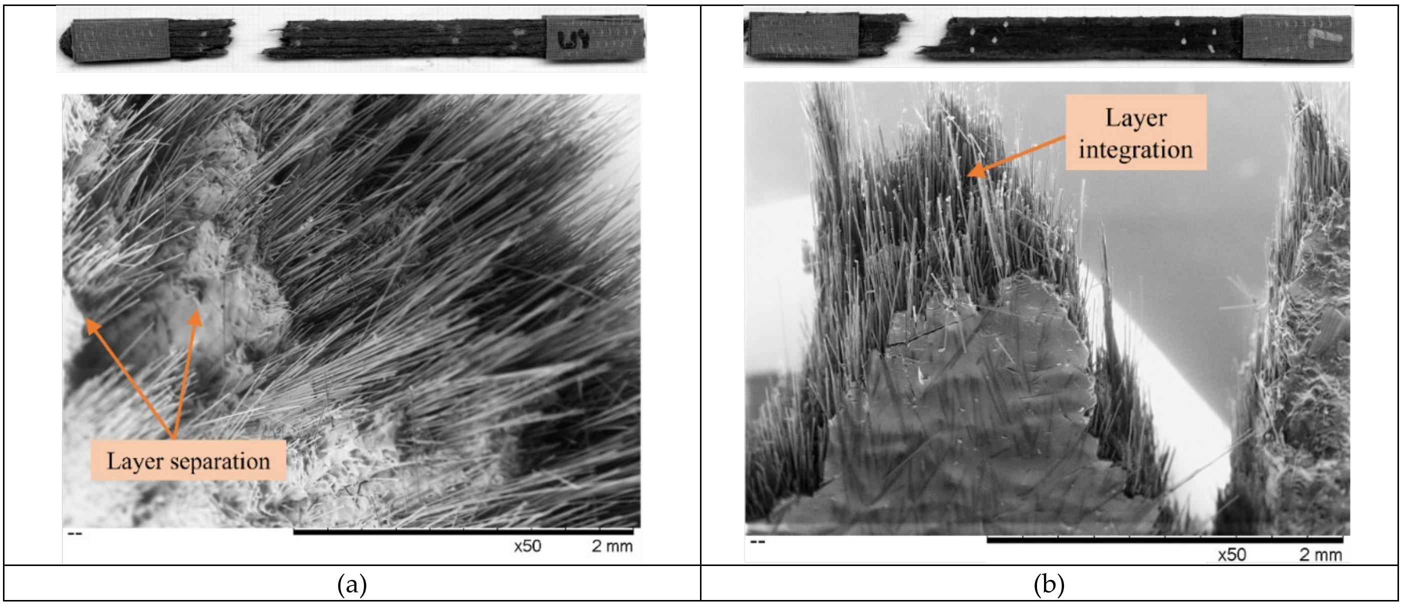

Figure 9 SEM image of tensile fracture surface: (a) as-printed; (b) post-printing consolidation

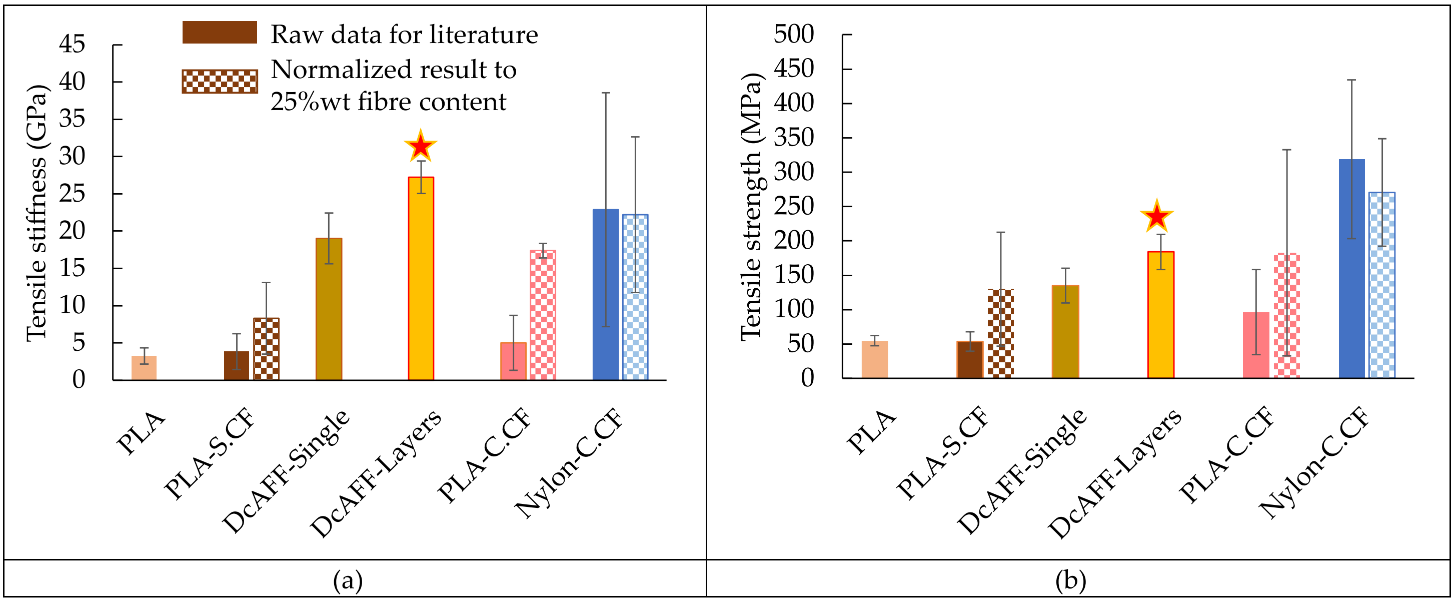

Figure 10 Comparison of tensile properties: (a) stiffness; (b) strength, between neat PLA [2,9,25-32], short carbon fibre-PLA (PLA-S.CF) [6,26,27,29,33-38], DcAFF-single layer as-printed [16], DcAFF multiple layers as-printed (the current test), continuous carbon fibre-PLA (PLA-C.CF) [39-43] and continuous carbon fibre nylon (Nylon-C.CF) [3,33,44-50], the whole composite sample was normalized with fibre weight content to 25% as the average fibre content of the current DcAFF in the checked pattern bar according to the literature data in Appendix A.

3.2. *Short beam shear testing (SBS)*

To investigate the multilayer printed material properties, short beam shear testing was selected. The test was adopted from ASTM D2344 [51]. According to the layer-by-layer manufacturing method of FFF, the interlaminar shear strength of the 3D printed part is an important property, so there were several studies focused on the short beam shear behaviour of 3D printed materials [1,2,52-55]. Moreover, heat treatments after 3D printing were also addressed in the literature to find the ultimate properties of the 3D printing part after the consolidation. The heat treatments can be performed from just above the glass transition temperature (70-80°C) to above the melting point (250°C) [52,55].

3.2.1. SBS specimen preparation and testing procedure

According to SBS specimen recommended size in ASTM D2344, *i.e.* testing span-to-thickness is 4, width-to-thickness is 2 and length-to-thickness is 6. The testing span was first selected to be 10 mm leading to the required thickness of 2.5 mm (eight layers of 0.3 mm) and width of 4 mm (four adjacent rasters on each layer). This approach was also taken in the literature [52,54,56]. The specimen was built with the same concentric printing procedure and length as the tensile specimen with an addition of four more layers. The 100-mm long specimen was then cut into four of 20-mm long specimens with a hack saw. The cut-end was then sanded and the dimensions of the specimens were measured. The average thicknesses and widths are 2.51±0.047 and 7.28±0.22 mm, respectively.

A group of the 8-layer, 100-mm long specimens was consolidated post-printing at the same condition as the tensile samples (200° for 1 hour under vacuum). Then, it was cut to the SBS size as specified by the standard. The top surface of the consolidated specimen (Figure 11(b)), presents no visible raster lines and is smoother than the as-printed part (Figure 11(a)). Voids in the specimen were removed after the consolidation as shown by the comparison in Figure 11(d) and (e). Similar to the tensile specimens' case, the SBS specimens after consolidation were 1.99±0.078 mm thick and 7.71±0.31 mm wide (20.7% thinner and 5.9% wider than the as-printed).

There were six tested samples in each group. The SBS was tested with the three-point bending method. The span support was set at 10 mm. The support and loading nose diameters were 3 and 4 mm, respectively. This is expected to distribute the load around the contact points. The displacement and the load were recorded. The testing was stopped when the displacement was larger than the thickness of the sample (2.5 mm) or the load drop-off was more than 30% of the maximum load. The short beam shear strength (F^{sbs}) was calculated from the maximum load (P_{max}) following Equation (1) where b and h are the width and thickness of the sample, respectively. The test setup is shown in Figure 11(e).

$$F^{sbs} = 0.75 \times \frac{P_{max}}{bxh} \quad (1)$$

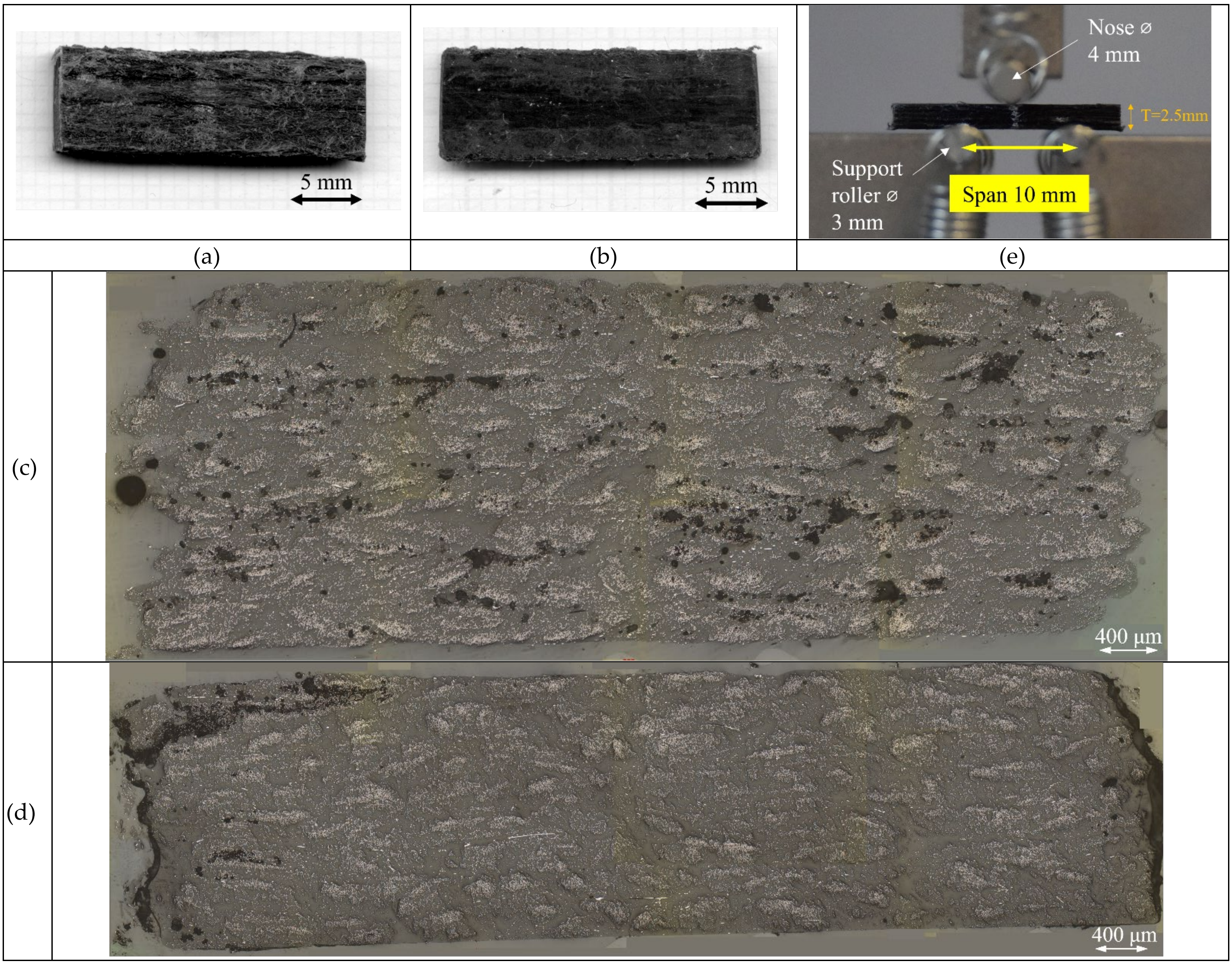

Figure 11 (a)-(b) Top view of SBS cut specimen as-printed and post-printing consolidation, (c)-(d) cross-section of 8-layer as-printed and consolidated specimen, (e) SBS test setup on the testing.

3.2.2. SBS testing result

Plots between SBS stress calculated from the load response with Equation (1) *versus* displacement of SBS as-printed and post-printing consolidation specimens are shown in Figure 12(a) and (b), respectively. The average SBS strength result of the as-printed and consolidated specimens are presented in Table 2. It can be seen that the as-printed has slightly lower SBS strength than the consolidated one while the stress-displacement response curves of the as-printed and the consolidated part are remarkably different. The as-printed part has no load drop after the initial failure/maximum load. This may be caused by the inelastic deformation that can be seen in the failed sample: the sample deformed plastically under the bending load. The inelastic deformation can cause a tensional crack on the bottom surface or a compressive crack on the top surface, as shown in Figure 13(a). This plateau stress-displacement curve and the inelastic deformation behaviour were also found in the literature of 3D printed SBS testing [1,52]. This inelastic failure may only be indicative of the general trends in the through-thickness behaviour of this material, but it cannot be interpreted as interlaminar shear strength. However, interlaminar failure is found in some failed samples, *e.g.* a partial interlaminar cracking on the side of a specimen Figure 13(b). On the other hand, the post-printing consolidated sample shows a sudden load drop after reaching the maximum load before slightly increasing again until the test is stopped.

This drop is a result of the brittle fracture of the compacted layers that causes the whole structure to fail at the same time. The failure of the post-printing consolidated sample can be a compressive failure on the top surface (Figure 14(a)), tensile cracking on the bottom surface or layer separation (Figure 14(b)). The consolidation can reduce the single-layer separation that can be seen in the as-printed part and change the failure behaviour of the sample.

The comparison of the as-printed DcAFF SBS strength to other composite 3D printed materials available in the literature, gathered in Appendix B, is shown in Figure 15. The DcAFF material shows higher SBS strength than the short carbon fibre PLA-based materials. This is the result of the long and aligned fibre in the HiPerDiF and the higher fibre content that strengthens the material, as seen in the tensile testing. DcAFF shows slightly lower properties compared to the nylon-continuous carbon fibre, Markforged. This is because of the different printing procedures of the Markforged which has dual nozzles feeding neat thermoplastic and impregnated fibre separately: the higher amount of thermoplastic on the outer specimen surfaces may enhance the raster fusion and increase the layer strength. Moreover, the continuous carbon fibre, the compatible fibre-nylon surface sizing, and the higher mechanical performance of nylon can also increase the strength of the material.

Table 2 SBS strength between as-printed and post-printing consolidated specimens

Conditions	Short beam shear strength (MPa)
As-printed	20.0 ± 1.2
Consolidated	25.0 ± 2.2

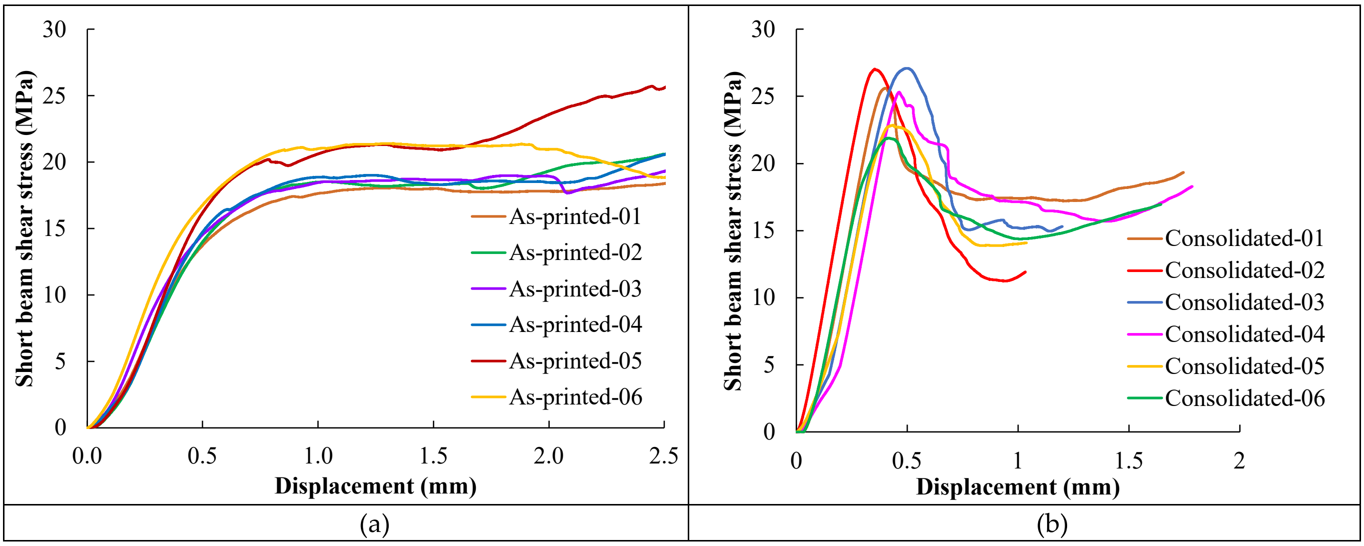

Figure 12 SBS stress *versus* displacement of the SBS testing: (a) as-printed; (b) post-printing consolidated sample

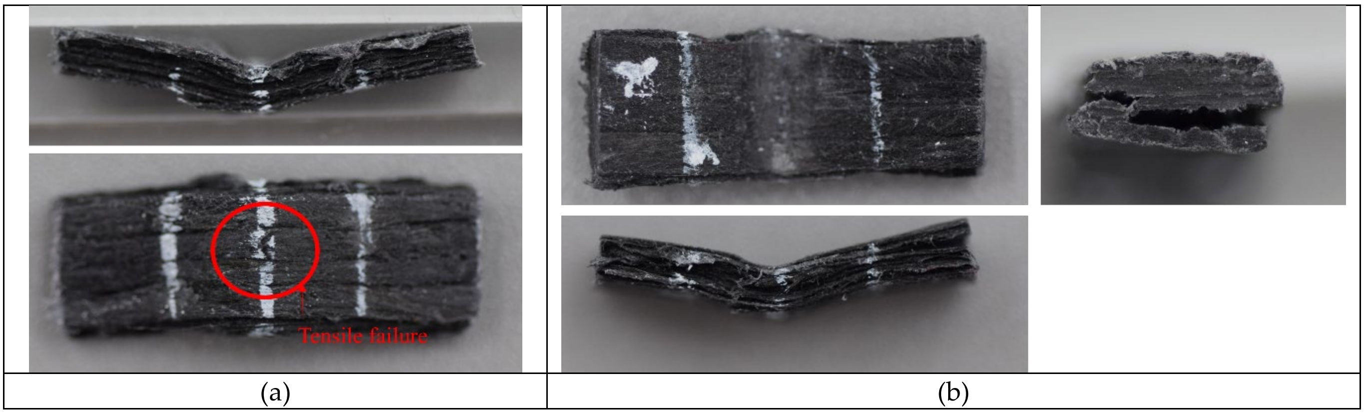

Figure 13 As-printed SBS failure sample: (a) tensile fracture on bottom side; (b) inelastic deformation with side layer separation.

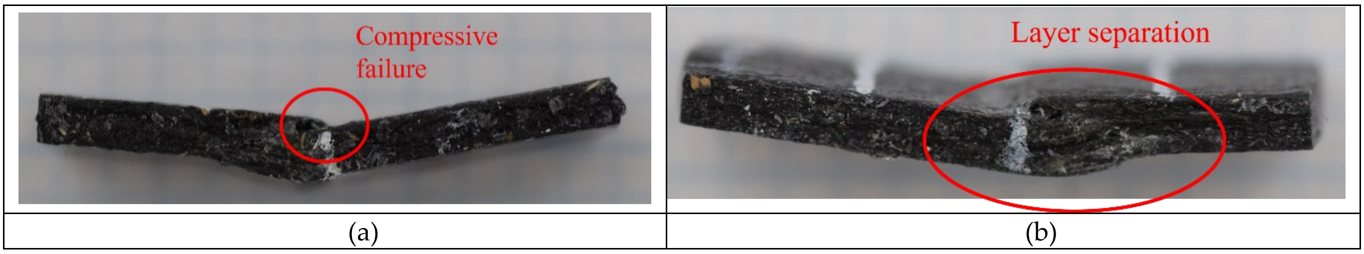

Figure 14 Post-printing consolidated SBS failure sample: (a) compressive failure on the top surface; (b) mid-layer separation with the kink on the top surface.

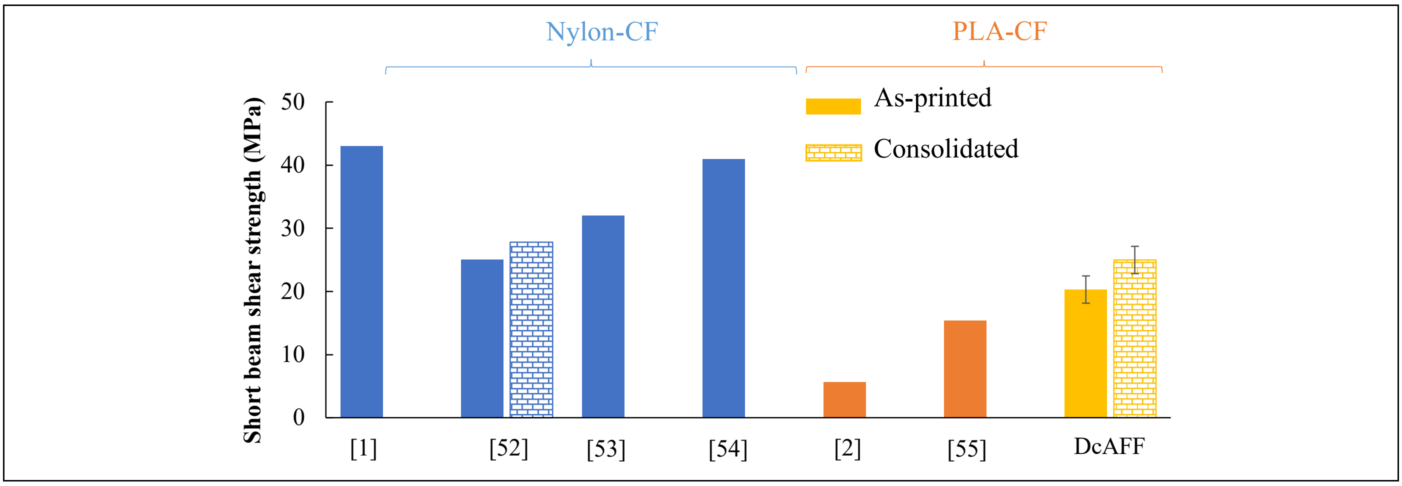

Figure 15 Comparison of the DcAFF SBS strength to other SBS testing in the literature of nylon-carbon fibre reinforcement [1,52-54] and PLA-carbon fibre reinforcement [2,55].

3.3. *Multilayer Open hole tensile testing*

Open-hole tensile properties of the DcAFF were tested and compared to the single-layer part from a previous paper [16]. The aim of the testing is not only to examine the performance of raster bonds in the presence of stress concentration but to study the capacity of the steering of the new filaments as well. In the previous studies [16], it has been observed that the single layer curvilinear 3D printed shape for open hole tensile testing changed the failure to non-catastrophic as the inter-raster breakage while the whole structure was still held together which cannot be seen when the hole was obtained with a material subtraction method. As seen in the multilayer tensile testing in section 3.1, multilayer 3D printing provides structural integrity that increases the overall mechanical performance of the part. Thus, the multilayer open-hole testing is expected to show some layer interaction that cannot be seen in the single layer. In this paper, the open-hole sample was fabricated with a similar shape, curvilinear printing path, used in a previous publication [16]. The path was designed including curvilinear, short, and long linear rasters, that allows to print the whole part in one go without stopping. The curvilinear printed path open hole behaviour will be compared with a multilayer linear 3D printed specimen with a drilled hole in the middle. According to the claim from many papers [57-59], the curvilinear 3D printing path on the open hole sample can provide composite steering with a higher fraction of continuous fibres aligned with the loading direction. The same argument could be applied to the case of discontinuous fibres given that their alignment provides continuous load transfer [57]. By contrast, the drilling will cut the fibre presenting a discontinuous load flow path which could lead to lower open-hole strength.

3.3.1. Open-hole tensile specimen preparation and testing

The curvilinear path from a previous study [15,16] was modified to complete one layer without stopping. There are four curvilinear rasters with four free-end rasters on each quarter of the circle. The free-end-rasters, called short rasters, are extended to attach to the circular curve to provide polymer adhesion. Eight straight rasters were built at the outer edge to strengthen the part. There are three superimposed layers of the same printing path. The curvilinear printing path and the printed sample are shown in Figure 16. The printed sample shows an eye-shape hole with a slightly smaller hole size than expected (~8 mm) due to the sliding of the raster on the printing bed as it is dragged by the nozzle during deposition. There are no important geometrical differences between the layers. The 3D printed part with the normal curvilinear, standard path, is called here "OPH-N"

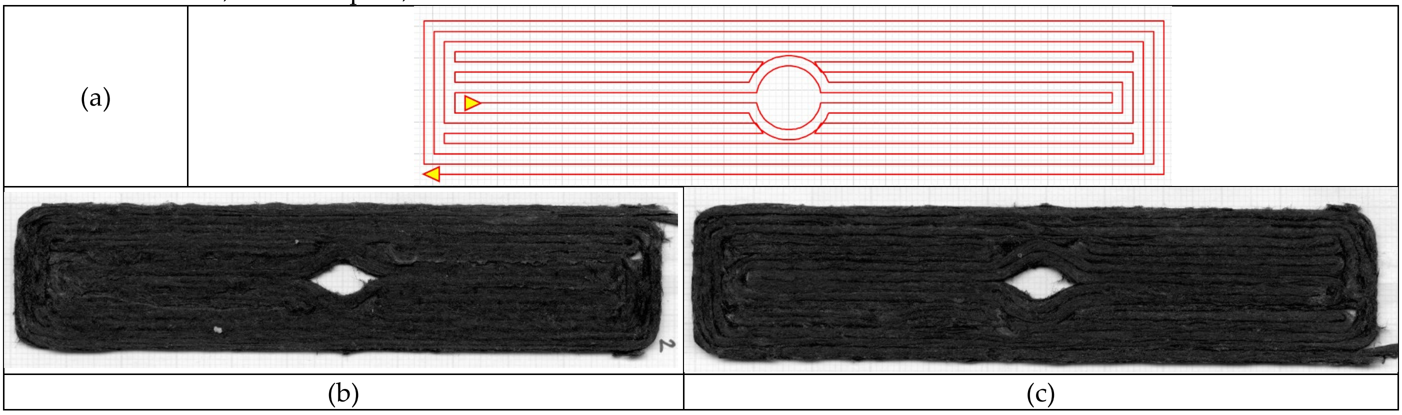

Figure 16 Normal curvilinear open hole printing (OPH-N): (a) continuous printing path; (b) and (c) example of the printed sample on top and bottom surface, respectively.

Owing to the poor hole shape, a modified path was introduced to improve the circularity of the hole and reduce the eye-shape effect. The movement of the raster should be caused by the imperfect bonding between the deposited raster and the printing bed because of the filleted end nozzle that leaves a 2-mm gap between the centre of the nozzle (reference point) and the position where the flat-end filleted nozzle can provide full pressure onto the deposited raster to generate adhesion on the printing bed. The imperfect printing was expected to be cancelled out by modifying the printing path by moving the nozzle further inward towards the centre of the hole to provide more contact to the bed at the entry and exit of the circular section. The modified printing path is shown in Figure 17(a). The overshooting length is 2 mm according to the estimated gap of the filleted nozzle. The top and bottom surfaces of the printed part are shown in Figure 17(b) and (c). The eye-shape corner at the attachment point disappears, but the hole is asymmetric due to the different behaviour between the movement at the entry and the exit of the circular section. This generates a sharp corner at the curvilinear entry, but a smooth curve at the exit due to the pulling on the raster because of the nozzle movement. The hole size is still smaller than the expectation, but it is closer to a circular hole than normal printing. This open-hole printed part with the modified path will be called "OPH-M".

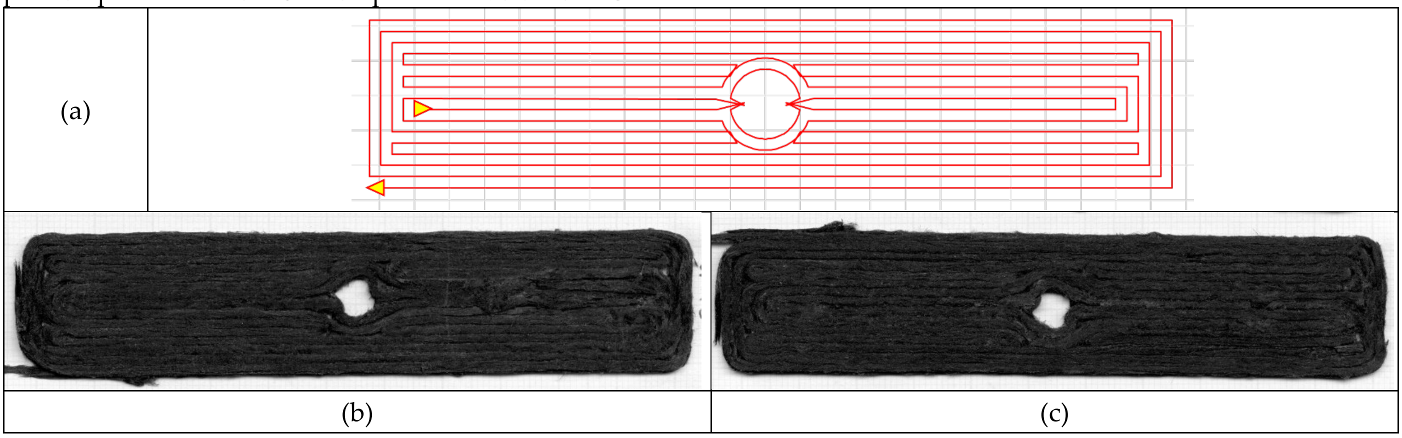

Figure 17 Modified curvilinear open hole printing: (a) modified printing path with the overshooting inward through the centre of the hole; (b) and (c) example of the printed sample on top and bottom surface.

The 3D-printed open hole will be benchmarked against the multilayer 3D printed with a drilled hole. The printing path is similar to the tensile specimen, but this part has more rasters in the layer than the tensile specimen. There are 16 rasters on one layer with three superimposing layers. After the printing, the centre position was marked and the hole was obtained *via* drilling. A 6-mm diameter carbide drilling bit was used in this case. The cutting speed is set at 2000 rpm and the feed rate is 1 mm per min. The drilled sample is shown in Figure 18. The sample with a drilled hole will be called "OPH-D".

The produced specimens' thickness and width were measured with a physical measurement, *i.e.* micrometre and calliper, while the hole size was measured *via* image processing of the scanned specimens. All samples were completed with 20-mm long end-tabs bonded onto both ends. The tensile testing was performed with the same procedure and machine used for the tensile testing. The strain was measured *via* digital image correlation (DIC) to obtain the strain map during loading. The DIC parameters are illustrated in Table 3. The stress was calculated across the cross-section at the hole area and the presented strain was calculated with the video extensometer feature of the DIC software.

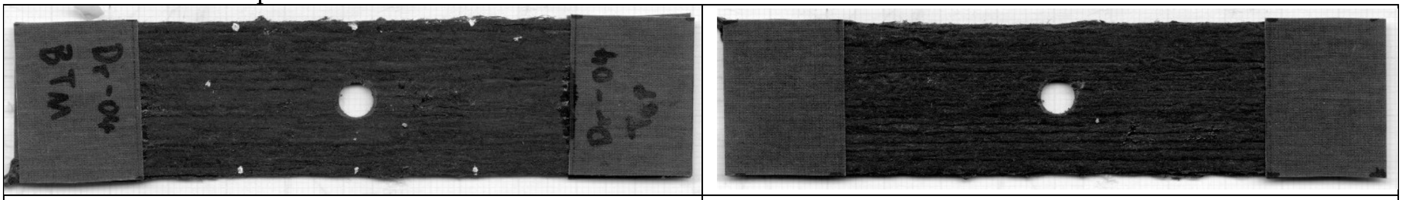

(a) (b)

Figure 18 Drilled sample on three layers 3D printed part: (a) top side; (b) bottom (bed) side.

Table 3 DIC technique parameters

Software	Davis10.1.2	**Image resolution**	2466 x 2092 pixel
Camera & Lens	M-lite & 50 mm	**Field of view**	75.78 mm x 64.28mm
Correlation mode	Relative to first	**Frame rate**	1 image per second
Subset size	51 x 51 Pixel (1.6 mm x 1.6 mm)	**Strain resolution**	2.33 x 10^{-04} ε
Step size	2 pixel (0.061 mm)	**Scale factor**	32.54 pixel/mm

3.3.2. Open-hole tensile test result

The load and displacement of the sample were recorded and converted to open-hole stress and strain across the hole section presented in Figure 19(a)-(c). The stress-strain curve of the three groups is linear in the first part and the slope decreases near the maximum load. This is slightly different from the single-layer stress-strain response of the 3D-printed open-hole testing in [16]: the multilayer has more linear behaviour than the single layer, and there is no load drop with increasing displacement. This may be because the multilayer, thicker cross-section and good bonding between layers and rasters, allows to store more energy in the part: when the failure point is reached, the energy is released to the whole structure causing the whole part to fail rather than gradually sacrificing the weak inter-raster bonding as in the single layer open hole part. The strength of the OPH-N multilayer is comparable with the single layer with the same printing procedure, around 80 MPa [16]. The strength of the specimens printed with the standard path is slightly lower than those with the modified one. This is because the modified path deposited slightly more material at the modified point than the standard printing. However, when comparing the three specimen groups shown in Figure 19(d), there are no statistical differences in the open hole strength. The similar strength may be caused by the same amount of the continuous raster through the length of the specimen. Moreover, there are four short linear rasters in the curvilinear part that are held to the other rasters by just the low-strength thermoplastic bonding. The number of short rasters is similar to the number of cut rasters due to the drill. Other printing procedures or post-printing processes may be considered to fill this gap, as seen in [57], and keep the number of continuous rasters as high as possible. The local strain map at the maximum load of each sample of the three groups for longitudinal (ε_x), transverse (ε_y) and shear (ε_{xy}) strains are shown in Figure 20.

In longitudinal strain (ε_x), the OPH-N shows high tensile strain at the contact points between the short raster and the curvilinear section. This is caused by the separation of the thermoplastic adhesion of the short rasters from the attached point on the curvilinear section. A separation between the curvilinear rasters is also found, but it is a lower longitudinal strain than the linear contact. This is caused by the worse bonding at the short-raster-end contact point than at the side-by-side raster. For the OPH-M sample, the strain distribution is asymmetrical around the hole. There is a high tensile strain on the curvilinear entry side that has a higher bending angle than the exit which has higher curvature. The high bending angle accumulated high stress at the turning corner while the curvilinear section has less stress accumulation. This presents as the different strain map on the opposite quarter of the circle. For the OPH-D sample, the longitudinal strain accumulated at the hole edge. This can be the cut of the raster that splits the rasters on the hole edge which is the weakest point in the part.

In the transverse direction (ε_y), the OPH-N shows a high tensile strain on the hole side where the linear raster attaches to the curvilinear raster. As a result of the low contact area at that point, the linear raster tends to separate from the curvilinear section. There is also a compression strain between the two attached middle rasters caused by Poisson's ratio effect. For the OPH-M, a high compression strain in the transverse direction is observed as a result of the tensile strain in the longitudinal direction. The short raster separation presents a high tensile strain in the transverse direction on the bottom left quarter. In the OPH-D, the remarkable strain is the compression strain between the rasters on the left of the hole. This is the result of the high tensile strain in the longitudinal direction on the right of the hole that reflects the crushing on the left as a hinge point in the structure. At this high strain point, the rasters may have poor adhesion, or the drill cut through the raster reducing raster strength.

In the shear strain (ε_{xy}), the OPH-N shows a symmetric shear strain between two halves of the hole caused by the separation of the short rasters from the curvilinear contact point. By contrast, the OPH-M shear strain distribution is asymmetric, presenting different strain distributions on each quarter of the hole, due to the asymmetric hole shape described above.

The failed samples, shown in Figure 21, comply with the strain map result. In the OPH-N sample, the crack started from the contact point of the short linear rasters and then it progressed through the diagonal direction producing a 45° failure on the opposite quarters. The breakage also ran through the curvilinear rasters after the initial failure. There is also a raster separation between the curvilinear rasters. In the OPH-M sample, the crack is similar to the OPH-N, but the final breakage is the linear breakage of the linear rasters. This is because the high strain progressed from the short raster contact point. The printed part can hold the structure together after the breakage. On the other hand, the drilled part (OPH-D) has a breakage through the hole perpendicular to the load direction, especially on the right of the hole, according to the high tensile strain in the longitudinal direction presented in Figure 20(c)).

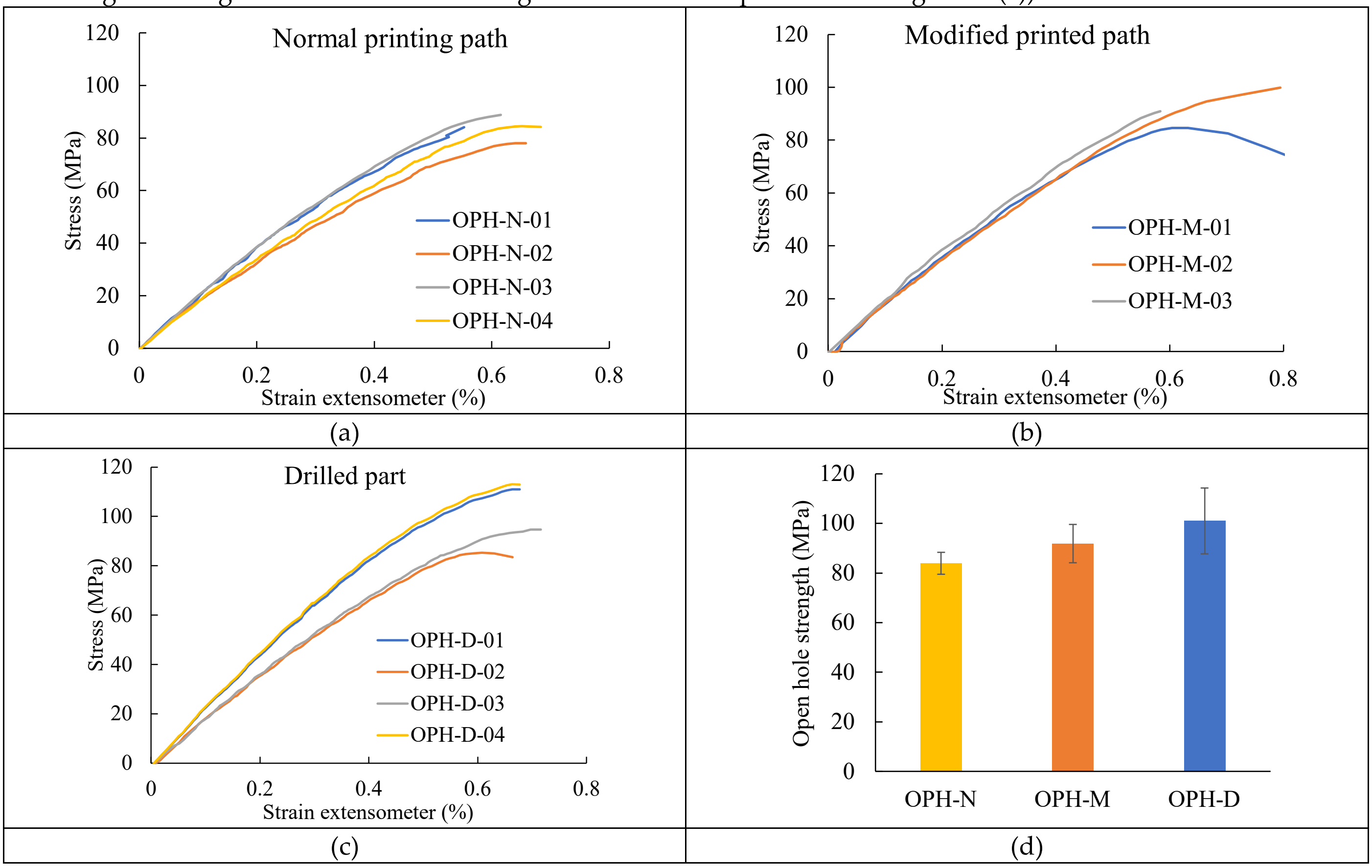

Figure 19 Open hole tensile testing result (a)-(c) stress-strain curve of open hole printed with normal curvilinear pat, open hole printed with modified curvilinear path and drill part, (d) open hole strength comparison between three groups of the sample.

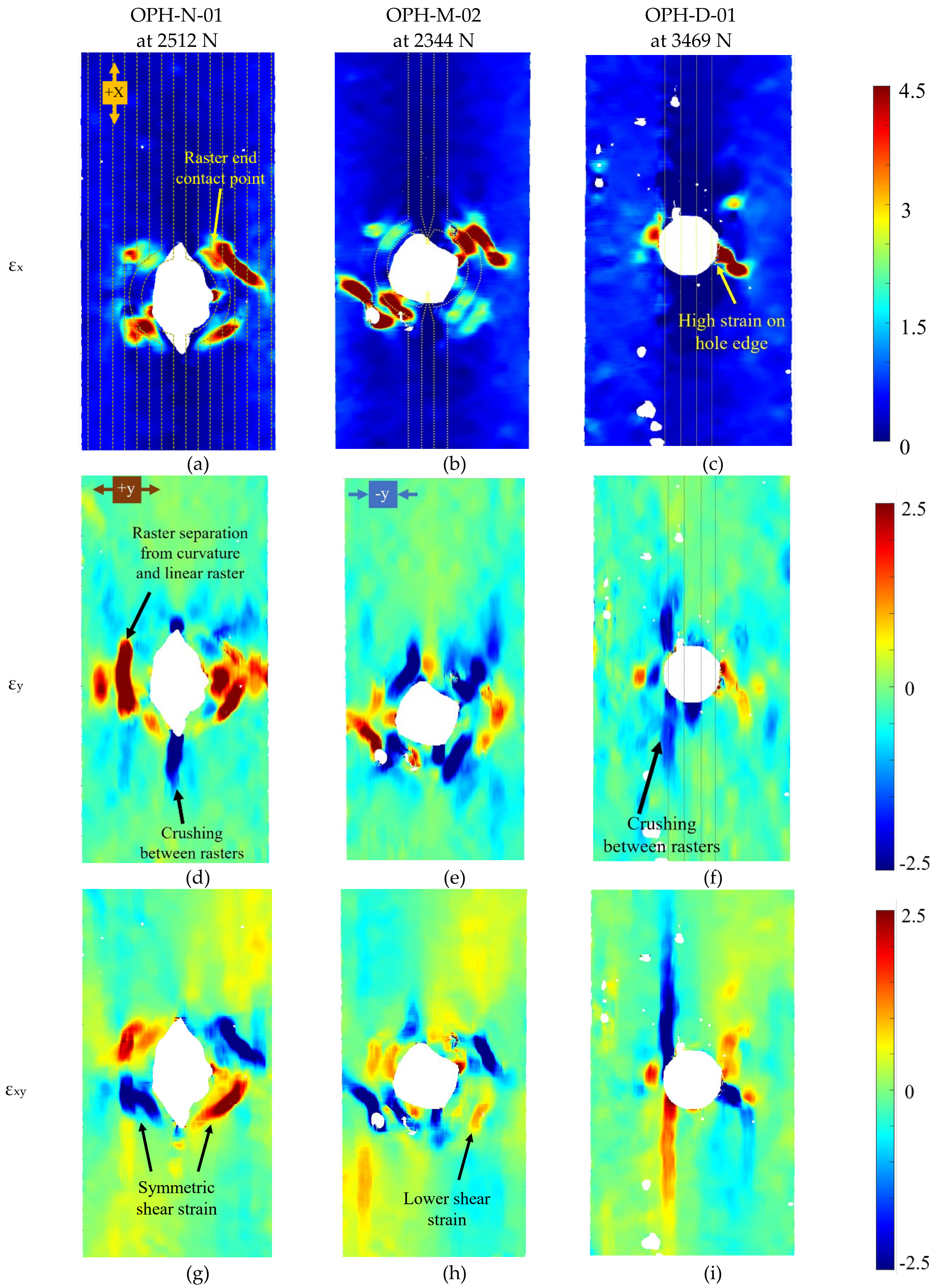

Figure 20 Strain map in longitudinal (ε_x), transverse (ε_y) and shear (ε_{xy}) at the maximum load of each sample analysed from DIC of open hole in different manufacturing scheme: normal printing (OPH-N), modified path (OPH-M), and drilled sample (OPH-D). 450 451 452

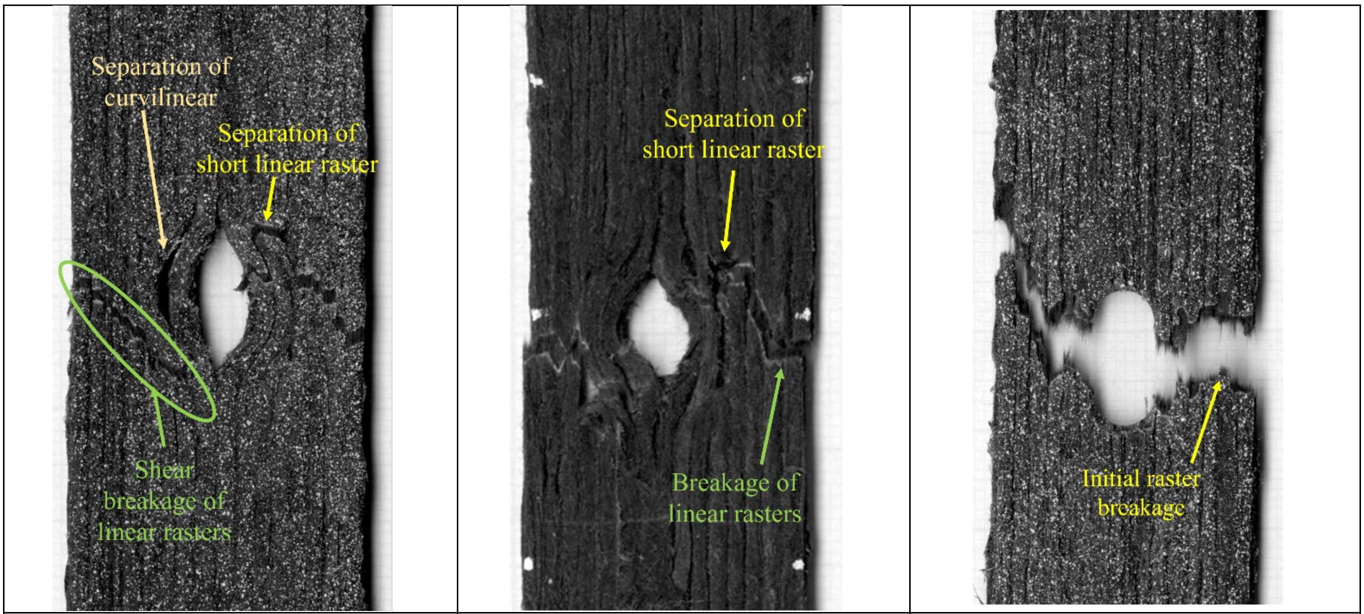

(a)	(b)	(c)

Figure 21 open hole tensile testing breakage sample: (a) OPH-N; (b) OPH-M; (c) OPH-D.

4. Conclusion

In this study, DcAFF material was produced at high production rate thanks to the development of the third-generation HiPerDiF machine. This allowed to study more 3D printing aspects, especially the interaction between layers that have never been studied before. Undefined material architecture characteristics, *i.e.* fibre alignment, of the produced DcAFF circular filament were investigated with an appropriate technique. The key findings and the discussion on each topic can be summarized as follows:

- The produced filament from the designed machine, roller bulking and pultrusion, resulted in a fine diameter circular DcAFF filament. The current filament has fibre weight content in the range of 20-30%, to promote adhesion to the printing bed and between rasters. The fibre alignment in the filament was studied by analysing µCT scanned images. The scanned images showed the development of the filament cross-section at the same location from the thin HiPerDiF film, passing through the roller bulking machine achieving a square-like cross section, and finally pultrusion to form a circular filament. The alignment calculation shows that the bulking process with the designed machine significantly increased fibre alignment in the filament. This led to the better mechanical performance of the filament than the thin tape.
- In tensile testing, the filament was printed into a four-layer tensile sample. The multilayer printing enhanced the bonding between the adjacent rasters delivering structural integrity resulting in higher tensile properties compared to the single-layer printing in a previous paper. The DcAFF also shows higher tensile properties than other PLA-composite 3D printing studies, even when normalised at the same fibre weight content. This is because of the alignment and the use of discontinuous fibres that give properties comparable to those of continuous fibre. The tensile properties can be increased further with the post-printing consolidation under heat and pressure. This process compressed the part and eliminated internal voids resulting in a united structure that changed the failure mechanism from layer separation to a breakage perpendicular to the load.
- The SBS testing was performed to show the interlayer properties of the material and the 3D printed part. The layer properties again can be increased with the post-printing consolidation that compacted the layer structure. Although there is no clear evidence of the interlaminar failure at the middle surface due to the high ductility of the material, the DcAFF shows a superior SBS strength to other carbon fibre PLA 3D printed parts from the literature.
- The performance of a more complex geometry printed with the DcAFF filament was studied with open-hole multilayer samples. Although the designed curvilinear printing path with short and continuous raster cannot compete with the strength of the drilled 3D printing part, the difference in the stress concentration of the curvilinear section may be beneficial when low-stress concentrations are required. Moreover, the

failure of the 3D printing part is less catastrophic than the drilled part. Even if the load drops more than 50% after the initial failure, the curvilinear part still stays together after the initial breakage.

Since DcAFF offers promising mechanical properties when printing multilayer, actually usable, parts, its development could be considered to be close to a commercialisation phase. However, some issues need to be addressed and studied:

- As can be seen in the complex geometry printing, *i.e.* the open-hole samples, the deposited rasters deviated from the defined path creating an eye-shaped hole instead of a circular one. This is the result of the poor bed adhesion and the too-tight turning radius of the printing path for the stiff 3-mm-long fibre in the 1 mm diameter composite filament. This discrepancy must be solved in future studies by *e.g.* the modification of the 3D printing parameters or printing path compensation.
- Although the tensile stiffness of the DcAFF can be considered to be competitive with commercially available 3D printing materials, this is not the case for tensile and SBS strength. This can be attributed to the easy-to-process, but low mechanical performance matrix, PLA, used in the current stage of filament development. Other high-performance thermoplastics, *e.g.* nylon, poly(ether ether ketone) (PEEK) or polyetherimide (PEI, ULTEM1000) with a higher amount of fibre content should be investigated to expand the application of the current DcAFF filament to more structural and commercial use.

Author Contributions: Conceptualization, all authors; methodology, N.K., M.L.; material preparation, N.K., M.L.; investigation, N.K., F.B., M.M.; data curation, N.K., F.B., M.M.; writing—original draft preparation, N.K., M.L., F.B.; writing—review and editing, all authors; supervision, M.L., I.H., B.W. and D.I.; All authors have read and agreed to the published version of the manuscript.

Funding: This work was supported by the Engineering and Physical Sciences Research Council (EPSRC) through the ACCIS Doctoral Training Centre [EP/L016028/1] and the EPSRC "High Performance Discontinuous Fibre Composites a sustainable route to the next generation of composites" [EP/P027393/1] grant. μ-CT scanning was supported by the National Research Facility for Lab X-ray CT (NXCT) at the μ-VIS X-ray Imaging Centre, University of Southampton, through EPSRC grant [EP/T02593X/1]. N.K. is supported by the Royal Thai Government scholarship provided by the Office of the Civil Service Commission (OCSC), Royal Government of Thailand.

Data Availability Statement: All data required for reproducibility are provided within the paper.

Acknowledgements: The authors thank Patrick Sullivan for conducting FARSEP fibre length measurement and also thank the support from μ-VIS X-ray Imaging Centre for the CT scanning and Bristol Composites Institute Laboratory Technical Support and Development Team for their constructive help and assistance.

Conflicts of Interest: The authors declare no conflict of interest. The funders had no role in the design of the study; in the collection, analyses, or interpretation of data; in the writing of the manuscript, or in the decision to publish the results.

Appendix A

The following tables, Table A 1-4, are the raw data gathered from the literature used for the comparison plotting in Figure 10.

Table A 1. Neat PLA tensile stiffness and strength collection from literature

Ref.	Stiffness (GPa)	Strength (MPa)
[2]	2.35	25.41
[9]	3.15	53.59
[25]	3.96	61.42
[26]	3.37	59.30
[27]	3.47	46.66
[31]	2.23	53.08
[28]	2.46	54.39
[29]	3.38	54.70
[30]	3.48	60.40
[32]	3.38	34.43
[36]	1.67	45.00

Table A 2. PLA - Short carbon fibre (PLA-S.CF) tensile stiffness and strength collection from literature

PLA-S.CF Ref.	Carbon Fibre content (%wt)	Raw data		Normalized with 25%wt	
		Stiffness (GPa)	Strength (MPa)	Stiffness (GPa)	Strength (MPa)
[29]	15	7.67	53.4	12.78	89.00
[6]	5	3.4	60	17.00	300.00
	10	5.2	70	13.00	175.00
	20	7.00	65	8.75	81.25
[26]	15	5.68	55.2	9.47	92.00
[27]	10	1.59	33.88	3.98	84.70
[38]	15	3.50	30.35	5.83	50.58
[34]	20	1.45	48.06	1.81	60.08
[35]	20	-	52	-	65.00
[37]	5	1.18	46.5	5.90	232.50
	10	1.77	77.8	4.43	194.50

Table A 3. PLA - Continuous carbon fibre (PLA-C.CF) tensile stiffness and strength collection from literature

PLA-C.CF Ref	Carbon Fibre content (%wt)	Raw data		Normalized with 25%wt	
		Stiffness (GPa)	Strength (MPa)	Stiffness (GPa)	Strength (MPa)
[39]	9.3	-	200	-	537.63
[40]	42.7	-	91	-	53.28
[43]	34.93	5.8	90	4.15	64.41
[41]	4.3	1.025	37	5.96	215.12
[42]	36.31	8.28	64.4	5.70	44.34

Table A 4. Nylon-Continuous carbon fibre (Nylon-C.CF, Markforged) tensile stiffness and strength collection from literature

Nylon-C.CF Ref	Carbon Fibre content (%wt)	Raw data		Normalized with 25%wt	
		Stiffness (GPa)	Strength (MPa)	Stiffness (GPa)	Strength (MPa)
[33]	36.67	10	341	6.82	232.48
[3]	36.13	51.7	436.7	35.77	302.17
	21.89	31.1	355.6	35.52	406.12
[44]	51.28	37	360	18.04	175.51
[45]	68.56	-	404.3	-	147.43
[60]	45.4	35.7	520	19.66	286.34
[46]	17.02	7.73	216	11.35	317.27
[50]	-	3.941	110	-	-
[47]	-	8.92	283.5	-	-
[48]	20.58	21.728	254.8	26.39	309.52
[49]	21.79	21.1	224.1	24.21	257.11

Appendix B

Table B1 is the raw data gathered from the literature of SBS testing with different material systems used for the SBS strength comparison plotting in Figure 15.

Table B1 Collection of 3D printed short beam shear (SBS) strength from literature

Ref.	Material	SBS strength	
		As-printed	Consolidated
[1]	Nylon-C.CF	43	-
[52]	Nylon-C.CF	25	27.8
[53]	Nylon-C.CF	32	-
[54]	Nylon-C.CF	40.9	-
[2]	PLA-S.CF	5.6	-
[55]	PLA-S.CF	15.38	-

5. References

1. O'Connor, H.J.; Dowling, D.P. Low‐pressure additive manufacturing of continuous fiber‐reinforced polymer composites. *Polymer Composites* **2019**, *40*, 4329-4339.
2. Vinoth Babu, N.; Venkateshwaran, N.; Rajini, N.; Ismail, S.O.; Mohammad, F.; Al-Lohedan, H.A.; Suchart, S. Influence of slicing parameters on surface quality and mechanical properties of 3D-printed CF/PLA composites fabricated by FDM technique. *Materials Technology* **2021**, 1-18.
3. Chacón, J.M.; Caminero, M.A.; Núñez, P.J.; García-Plaza, E.; García-Moreno, I.; Reverte, J.M. Additive manufacturing of continuous fibre reinforced thermoplastic composites using fused deposition modelling: Effect of process parameters on mechanical properties. *Composites Science and Technology* **2019**, *181*, 107688, doi:https://doi.org/10.1016/j.compscitech.2019.107688.
4. Ngo, T.D.; Kashani, A.; Imbalzano, G.; Nguyen, K.T.Q.; Hui, D. Additive manufacturing (3D printing): A review of materials, methods, applications and challenges. *Composites Part B: Engineering* **2018**, *143*, 172-196, doi:https://doi.org/10.1016/j.compositesb.2018.02.012.
5. Yang, C.; Tian, X.; Liu, T.; Cao, Y.; Li, D. 3D printing for continuous fiber reinforced thermoplastic composites: mechanism and performance. *Rapid Prototyping Journal* **2017**, *23*, 209-215, doi:https://doi.org/10.1108/RPJ-08-2015-0098.
6. Sang, L.; Han, S.; Li, Z.; Yang, X.; Hou, W. Development of short basalt fiber reinforced polylactide composites and their feasible evaluation for 3D printing applications. *Composites Part B: Engineering* **2019**, *164*, 629-639, doi:https://doi.org/10.1016/j.compositesb.2019.01.085.
7. Wu, W.; Geng, P.; Li, G.; Zhao, D.; Zhang, H.; Zhao, J. Influence of layer thickness and raster angle on the mechanical properties of 3D-printed PEEK and a comparative mechanical study between PEEK and ABS. *Materials* **2015**, *8*, 5834-5846, doi:https://doi.org/10.3390/ma8095271.
8. Perez, A.R.T.; Roberson, D.A.; Wicker, R.B. Fracture surface analysis of 3D-printed tensile specimens of novel ABS-based materials. *Journal of Failure Analysis and Prevention* **2014**, *14*, 343-353, doi:https://doi.org/10.1007/s11668-014-9803-9.
9. Lanzotti, A.; Pei, E.; Grasso, M.; Staiano, G.; Martorelli, M. The impact of process parameters on mechanical properties of parts fabricated in PLA with an open-source 3-D printer. *Rapid Prototyping Journal* **2015**, *21*, 604-617, doi:https://doi.org/10.1108/RPJ-09-2014-0135.
10. Liao, G.; Li, Z.; Cheng, Y.; Xu, D.; Zhu, D.; Jiang, S.; Guo, J.; Chen, X.; Xu, G.; Zhu, Y. Properties of oriented carbon fiber/polyamide 12 composite parts fabricated by fused deposition modeling. *Materials & Design* **2018**, *139*, 283-292, doi:https://doi.org/10.1016/j.matdes.2017.11.027.
11. Tian, X.; Liu, T.; Yang, C.; Wang, Q.; Li, D. Interface and performance of 3D printed continuous carbon fiber reinforced PLA composites. *Composites Part A: Applied Science and Manufacturing* **2016**, *88*, 198-205, doi:https://doi.org/10.1016/j.compositesa.2016.05.032.
12. Krajangsawasdi, N.; Blok, L.G.; Hamerton, I.; Longana, M.L.; Woods, B.K.S.; Ivanov, D.S. Fused Deposition Modelling of Fibre Reinforced Polymer Composites: A Parametric Review. *Journal of Composites Science* **2021**, *5*, 29.

13. Blok, L.G.; Longana, M.L.; Woods, B.K.S. Fabrication and characterisation of aligned discontinuous carbon fibre reinforced thermoplastics for automated manufacture. *Materials* **2020**, *13*, 4671, doi:https://doi.org/10.3390/ma13204671.
14. Krajangsawasdi, N.; Longana, M.L.; Hamerton, I.; Woods, B.K.; Ivanov, D.S. Batch production and fused filament fabrication of highly aligned discontinuous fibre thermoplastic filaments. *Additive Manufacturing* **2021**, *48*, 102359.
15. Krajangsawasdi, N.; Woods, B.K.S.; Hamerton, I.; Ivanov, D.S.; Longana, M.L. Highly Aligned Discontinuous Fibre Composite Filaments for Fused Deposition Modelling: Open-Hole Case Study. In Proceedings of the Composites Meet Sustainability – Proceedings of the 20th European Conference on Composite Materials, ECCM20, Lausanne, Switzerland, 26–30 June 2022, 2022.
16. Krajangsawasdi, N.; Hamerton, I.; Woods, B.K.S.; Ivanov, D.S.; Longana, M.L. Open Hole Tension of 3D Printed Aligned Discontinuous Composites. *Materials* **2022**, *15*, 8698.
17. Such, M.; Ward, C.; Potter, K. Aligned discontinuous fibre composites: a short history. *Journal of Multifunctional Composites* **2014**, *2*, 155-168.
18. Yee, R.; Stephens, T. A TGA technique for determining graphite fiber content in epoxy composites. *Thermochimica Acta* **1996**, *272*, 191-199.
19. Yu, H.; Potter, K.D.; Wisnom, M.R. A novel manufacturing method for aligned discontinuous fibre composites (High Performance-Discontinuous Fibre method). *Composites Part A: Applied Science and Manufacturing* **2014**, *65*, 175-185, doi:https://doi.org/10.1016/j.compositesa.2014.06.005.
20. Tang, J.; Swolfs, Y.; Longana, M.L.; Yu, H.; Wisnom, M.R.; Lomov, S.V.; Gorbatikh, L. Hybrid composites of aligned discontinuous carbon fibers and self-reinforced polypropylene under tensile loading. *Composites Part A: Applied Science and Manufacturing* **2019**, *123*, 97-107.
21. Straumit, I.; Lomov, S.V.; Wevers, M. Quantification of the internal structure and automatic generation of voxel models of textile composites from X-ray computed tomography data. *Composites Part A: Applied Science and Manufacturing* **2015**, *69*, 150-158.
22. Yang, D.; Zhang, H.; Wu, J.; McCarthy, E.D. Fibre flow and void formation in 3D printing of short-fibre reinforced thermoplastic composites: An experimental benchmark exercise. *Additive Manufacturing* **2021**, *37*, 101686.
23. Hartwich, M.; Höhn, N.; Mayr, H.; Sandau, K.; Stengler, R. *FASEP ultra-automated analysis of fibre length distribution in glass-fibre-reinforced products*; SPIE: 2009; Volume 7389.
24. Gardner, J.M.; Sauti, G.; Kim, J.-W.; Cano, R.J.; Wincheski, R.A.; Stelter, C.J.; Grimsley, B.W.; Working, D.C.; Siochi, E.J. *Additive Manufacturing of Multifunctional Components using High Density Carbon Nanotube Yarn Filaments*; NASA Langley Research Center: Hampton, VA, 2016.
25. Song, Y.; Li, Y.; Song, W.; Yee, K.; Lee, K.-Y.; Tagarielli, V.L. Measurements of the mechanical response of unidirectional 3D-printed PLA. *Materials & Design* **2017**, *123*, 154-164, doi:https://doi.org/10.1016/j.matdes.2017.03.051.
26. Ivey, M.; Melenka, G.W.; Carey, J.P.; Ayranci, C. Characterizing short-fiber-reinforced composites produced using additive manufacturing. *Advanced Manufacturing: Polymer & Composites Science* **2017**, *3*, 81-91, doi:https://doi.org/10.1080/20550340.2017.1341125.
27. Vinyas, M.; Athul, S.; Harursampath, D. Mechanical characterization of the Poly lactic acid (PLA) composites prepared through the Fused Deposition Modelling process. *Materials Research Express* **2019**, *6*, 105359.
28. Wang, X.; Jiang, M.; Zhou, Z.; Gou, J.; Hui, D. 3D printing of polymer matrix composites: A review and prospective. *Composites Part B: Engineering* **2017**, *110*, 442-458, doi:https://doi.org/10.1016/j.compositesb.2016.11.034.
29. Ferreira, R.T.L.; Amatte, I.C.; Dutra, T.A.; Burger, D. Experimental characterization and micrography of 3D printed PLA and PLA reinforced with short carbon fibers. *Composites Part B: Engineering* **2017**, *124*, 88-100, doi:https://doi.org/10.1016/j.compositesb.2017.05.013.

30. Tymrak, B.; Kreiger, M.; Pearce, J.M. Mechanical properties of components fabricated with open-source 3-D printers under realistic environmental conditions. *Materials & Design* **2014**, *58*, 242-246.
31. Yao, T.; Ye, J.; Deng, Z.; Zhang, K.; Ma, Y.; Ouyang, H. Tensile failure strength and separation angle of FDM 3D printing PLA material: Experimental and theoretical analyses. *Composites Part B: Engineering* **2020**, *188*, 107894.
32. Cicala, G.; Giordano, D.; Tosto, C.; Filippone, G.; Recca, A.; Blanco, I. Polylactide (PLA) filaments a biobased solution for additive manufacturing: Correlating rheology and thermomechanical properties with printing quality. *Materials* **2018**, *11*, 1191, doi:https://doi.org/10.3390/ma11071191.
33. Isobe, T.; Tanaka, T.; Nomura, T.; Yuasa, R. Comparison of strength of 3D printing objects using short fiber and continuous long fiber. In Proceedings of the 13th International Conference on Textile Composites (TEXCOMP-13), Milan, Italy, 17–19 September 2018, 2018; p. 012042.
34. Omer, R.; Mali, H.S.; Singh, S.K. Tensile performance of additively manufactured short carbon fibre-PLA composites: neural networking and GA for prediction and optimisation. *Plastics, Rubber and Composites* **2020**, *49*, 271-280.
35. Ding, Q.; Li, X.; Zhang, D.; Zhao, G.; Sun, Z. Anisotropy of poly (lactic acid)/carbon fiber composites prepared by fused deposition modeling. *Journal of Applied Polymer Science* **2020**, *137*, 48786, doi:https://doi.org/10.1002/app.48786.
36. Papon, M.E.A.; Haque, A.; MA, R.S. Effect of nozzle geometry on melt flow simulation and structural property of thermoplastic nanocomposites in fused deposition modeling. In Proceedings of the the American Society for Composites, Thirty-Second Technical Conference, West Lafayette, IN, USA, , 23–25 October 2017, 2017.
37. Giani, N.; Mazzocchetti, L.; Benelli, T.; Picchioni, F.; Giorgini, L. Towards sustainability in 3D printing of thermoplastic composites: evaluation of recycled carbon fibers as reinforcing agent for FDM filament production and 3D printing. *Composites Part A: Applied Science and Manufacturing* **2022**, 107002.
38. El Magri, A.; El Mabrouk, K.; Vaudreuil, S.; Ebn Touhami, M. Mechanical properties of CF-reinforced PLA parts manufactured by fused deposition modeling. *Journal of Thermoplastic Composite Materials* **2021**, *34*, 581-595.
39. Matsuzaki, R.; Ueda, M.; Namiki, M.; Jeong, T.-K.; Asahara, H.; Horiguchi, K.; Nakamura, T.; Todoroki, A.; Hirano, Y. Three-dimensional printing of continuous-fiber composites by in-nozzle impregnation. *Scientific reports* **2016**, *6*, 23058, doi:https://doi.org/10.1038/srep23058.
40. Li, N.; Li, Y.; Liu, S. Rapid prototyping of continuous carbon fiber reinforced polylactic acid composites by 3D printing. *Journal of Materials Processing Technology* **2016**, *238*, 218-225, doi:https://doi.org/10.1016/j.jmatprotec.2016.07.025.
41. Chaudhry, F.N.; Butt, S.I.; Mubashar, A.; Naveed, A.B.; Imran, S.H.; Faping, Z. Effect of carbon fibre on reinforcement of thermoplastics using FDM and RSM. *Journal of Thermoplastic Composite Materials* **2022**, *35*, 352-374.
42. Heidari-Rarani, M.; Rafiee-Afarani, M.; Zahedi, A. Mechanical characterization of FDM 3D printing of continuous carbon fiber reinforced PLA composites. *Composites Part B: Engineering* **2019**, *175*, 107147.
43. Namiki, M.; Ueda, M.; Todoroki, A.; Hirano, Y. 3D printing of continuous fiber reinforced plastic. In Proceedings of the SAMPE 2014, International SAMPE Symposium and Exhibition, Seattle, WA, USA, 2–5 June 2014, 2014.
44. Al Abadi, H.; Thai, H.-T.; Paton-Cole, V.; Patel, V.I. Elastic properties of 3D printed fibre-reinforced structures. *Composite Structures* **2018**, *193*, 8-18, doi:https://doi.org/10.1016/j.compstruct.2018.03.051.
45. Mohammadizadeh, M.; Imeri, A.; Fidan, I.; Elkelany, M. 3D printed fiber reinforced polymer composites-Structural analysis. *Composites Part B: Engineering* **2019**, *175*, 107112, doi:https://doi.org/10.1016/j.compositesb.2019.107112.
46. Dickson, A.N.; Barry, J.N.; McDonnell, K.A.; Dowling, D.P. Fabrication of continuous carbon, glass and Kevlar fibre reinforced polymer composites using additive manufacturing. *Additive Manufacturing* **2017**, *16*, 146-152, doi:https://doi.org/10.1016/j.addma.2017.06.004.
47. Agarwal, K.; Kuchipudi, S.K.; Girard, B.; Houser, M. Mechanical properties of fiber reinforced polymer composites: A comparative study of conventional and additive manufacturing methods. *Journal of Composite Materials* **2018**, *52*, 3173-3181.

48. Oztan, C.; Karkkainen, R.; Fittipaldi, M.; Nygren, G.; Roberson, L.; Lane, M.; Celik, E. Microstructure and mechanical properties of three dimensional-printed continuous fiber composites. *Journal of Composite Materials* **2019**, *53*, 271-280.
49. Sanei, S.H.R.; Lash, Z.; Servey, J.; Gardone, F.; Nikhare, C.P. Mechanical properties of 3D printed fiber reinforced thermoplastic. In Proceedings of the ASME International Mechanical Engineering Congress and Exposition, 2019; p. V012T010A016.
50. Mei, H.; Ali, Z.; Ali, I.; Cheng, L. Tailoring strength and modulus by 3D printing different continuous fibers and filled structures into composites. *Advanced Composites and Hybrid Materials* **2019**, *2*, 312-319.
51. international, A. *ASTM D2344/D2344M-22 Standard Test Method for Short-Beam Strength of Polymer Matrix Composite Materials and Their Laminates*; 16 August 2022 2022; p. 10.
52. Pascual-González, C.; San Martín, P.; Lizarralde, I.; Fernández, A.; León, A.; Lopes, C.; Fernández-Blázquez, J. Post-processing effects on microstructure, interlaminar and thermal properties of 3D printed continuous carbon fibre composites. *Composites Part B: Engineering* **2021**, *210*, 108652.
53. Caminero, M.; Chacón, J.M.; García-Moreno, I.; Rodríguez, G.P. Impact damage resistance of 3D printed continuous fibre reinforced thermoplastic composites using fused deposition modelling. *Composites Part B: Engineering* **2018**, *148*, 93-103, doi:https://doi.org/10.1016/j.compositesb.2018.04.054.
54. Yavas, D.; Zhang, Z.; Liu, Q.; Wu, D. Interlaminar shear behavior of continuous and short carbon fiber reinforced polymer composites fabricated by additive manufacturing. *Composites Part B: Engineering* **2021**, *204*, 108460.
55. Papon, E.A.; Haque, A.; Spear, S.K. Effects of functionalization and annealing in enhancing the interfacial bonding and mechanical properties of 3D printed fiber-reinforced composites. *Materials Today Communications* **2020**, *25*, 101365.
56. Wang, X.; Zhao, X.; Wu, Z.; Zhu, Z.; Wang, Z. Interlaminar shear behavior of basalt FRP and hybrid FRP laminates. *Journal of Composite Materials* **2016**, *50*, 1073-1084.
57. Zhang, H.; Li, A.; Wu, J.; Sun, B.; Wang, C.; Yang, D. Effectiveness of fibre placement in 3D printed open-hole composites under uniaxial tension. *Composites Science and Technology* **2022**, *220*, 109269.
58. Li, N.; Link, G.; Wang, T.; Ramopoulos, V.; Neumaier, D.; Hofele, J.; Walter, M.; Jelonnek, J. Path-designed 3D printing for topological optimized continuous carbon fibre reinforced composite structures. *Composites Part B: Engineering* **2020**, *182*, 107612.
59. Khan, S.; Fayazbakhsh, K.; Fawaz, Z.; Nik, M.A. Curvilinear variable stiffness 3D printing technology for improved open-hole tensile strength. *Additive Manufacturing* **2018**, *24*, 378-385.
60. Van Der Klift, F.; Koga, Y.; Todoroki, A.; Ueda, M.; Hirano, Y.; Matsuzaki, R. 3D printing of continuous carbon fibre reinforced thermo-plastic (CFRTP) tensile test specimens. *Open Journal of Composite Materials* **2016**, *6*, 18-27, doi:http://dx.doi.org/10.4236/ojcm.2016.61003.